*SACLANT UNDERSEA
RESEARCH CENTRE
REPORT*

BOTTOM REVERBERATION IN SHALLOW WATER: COHERENT PROPERTIES AS A FUNCTION OF BANDWITH, WAVEGUIDE CHARACTERISTICS AND SCATTERER DISTRIBUTIONS

LePage, K.D

October 1998

20000502 058

Bottom reverberation in shallow water: coherent properties as a function of bandwidth, waveguide characteristics and scatterer distributions

Kevin D. LePage

The content of this document pertains to work performed under Project 042-4 of the SACLANTCEN Programme of Work. The document has been approved for release by The Director, SACLANTCEN.

Jan L. Spoelstra
Director

intentionally blank page

**Bottom reverberation in shallow water:
coherent properties as a function of
bandwidth, waveguide characteristics
and scatterer distributions**

Kevin D. LePage

Executive Summary: Shallow water presents a difficult environment for finding submarines. Since shallow water is typically a reverberation limited environment, it is important to understand the predictable structure of the reverberation in order to aid the design of processors and detectors which work properly in these environments. In this report, the temporal characteristics of monostatic reverberation are predicted as a function of source bandwidth, source-receiver depth, and the propagation characteristics of shallow water. Results show that at early time, reverberation can be highly coherent across a vertical line array, violating the homogeneous noise assumption, while at late time the reverberation becomes increasingly uncorrelated. This is shown to be due to the ensonification of independent bottom patches at late time. It is also shown that this decorrelation of the reverberation is dependent on the propagation characteristics of the particular shallow water environment, the correlation length scale of the scatterers, and the bandwidth of the source, with high bandwidth sources causing decorrelated reverberation sooner than low bandwidth sources. The results also show that there are several identifying characteristics in reverberation time series which may be useful for identifying the types of scatterers which cause reverberation during particular experiments. Finally, the techniques developed in this report may be used to generate reverberation time series from scatterers obeying different amplitude and spatial distributions. This ability should be used in the future to help understand whether it is possible to simulate the conditions under which reverberation becomes non-Rayleigh, as has been observed experimentally by the Centre in recent experiments.

intentionally blank page

Bottom reverberation in shallow water: coherent properties as a function of bandwidth, waveguide characteristics and scatterer distributions

Kevin D. LePage

Abstract: Scattering physics are often modeled using the Helmholtz equation for computational reasons. Likewise, propagation loss to and from scattering regions are often treated in a like manner. The usual approach for generating reverberation time series therefore requires a numerical Fourier synthesis which can obscure the physics of reverberation phenomenology. Here we model the reverberation process approximately using normal modes and perform the Fourier synthesis explicitly under a narrow band approximation. The modes are allowed to interact with the bottom individually, but the interaction of the modes at the bottom is also retained. Therefore the approach allows pathological propagation phenomena such as convergence zones to be explicitly modeled. As a natural result of the broadband nature of the analysis, the interaction of the modes with each other at the bottom is seen to be governed by the bandwidth of the analysis and the dispersive properties of the waveguide. The result is that modes which interact coherently at bottom patches at early time may decorrelate at late times, in ways which are determined by the mean propagation physics of the waveguide and the reverberation analysis band.

In the interests of keeping the approach as general as possible, the physics of the bottom scattering process are specified by the user. These physics are supplied in the form of local bottom scattering functions, which will generally be related to the mode shape functions and their derivatives at and in the bottom, which are sensitive to the detailed bottom structure and the incident grazing angles of each mode. This approach makes it possible to model several of the more popular bottom scattering models, such as perturbation theory and Lambert's law, within the framework of a general reverberation model. All scattering is assumed to be weak, so that a small imaginary part of the model eigenvalues is sufficient to account for energy loss due to scattering, and local, so that the field scattered at any particular part of the bottom is due only to the bottom properties at that particular point. This latter approximation serves as a restriction on the ability of the model to accommodate large scale scatterers such as facets or other target type features, but is useful for modeling clutter, the intended objective.

Keywords: reverberation ∘ scattering ∘ narrowband

Contents

1

Introduction

Reverberation at a given time is modeled as coherent propagation over a sum of normal modes to all candidate bottom locations, a local interaction with some sediment or subbottom process at each candidate location, and deterministic propagation over a second sum of normal modes back to the receiver. Given the physics of wave-guide propagation and the bandwidth of the processing, certain parts of the bottom will yield the bulk of the backscattered return at any given time. These ranges are generally assumed to be determined by the relation

$$r = ct/2.$$

In the following it will be shown that the simple relation given above for the scatterer range should in reality be replaced by the time over the sum of the modal group slownesses $S_{n,m}$ for the mode pair of interest at the center frequency of interest. The modal group slownesses in turn are the inverse group speeds $\partial k_{n,m}/\partial \omega$, a parameter which is intimately related to the narrow band approximation used throughout this report.

The geometry is monostatic in the horizontal coordinates, although different depths of the source and the receiver may be accommodated. As a generalization, different source and receiver vertical apertures and receiver characteristics may also be accommodated, although they are not explicitly treated in this report. The bottom scatterers themselves are assumed to be a homogeneous distribution with isotropic Gaussian correlation properties.

This work follows in the footsteps of two other normal mode reverberation treatments, one of which is embodied in the reverberation model developed at SAC-LANTCEN by Dale Ellis [1], and the other of which is a more similar treatment for volume inhomogeneity scatter in a shallow water waveguide developed by D. J. Tang [2]. This treatment differs from the ones which came before in that more emphasis is placed on the importance of modal interaction, and consequently a better understanding of when the modal components of the backscattered field are coherent or are not coherent has been developed. The theory developed here also explores the time dependent properties of spatial coherence and explores how the ratio of the bottom patch size to the correlation length scale of the scatterers affects the resonant scattering characteristics of the reverberation.

2

Theory

Under the far field approximation, the total field "incident" from a point source to a scatterer on or in the bottom at range r and frequency ω is given approximately by

$$p_i(\omega, z_s, r) \simeq \sqrt{\frac{2\pi}{r}} \sum_{m=1}^{N} \frac{\phi_m(z_s)\phi_m^-}{\sqrt{k_m}} e^{ik_m r}, \tag{1}$$

where the k_m are the modal wavenumbers, the ϕ_m the mode shape functions and z_s is the source depth.

In Eq. (1), the scattering function ϕ_m^- is intended to represent the excitation of some sediment or subbottom scatterer by mode m. For instance, in the simplest rough surface perturbation theory, the excitation of a scatterer is linear in the scatterer size and the difference between the normal derivative of the mode shape function over the boundary impedance and the second derivative at the scattering boundary (see Annex D for details of the derivation)

$$\phi_{m,perturbation}^- \simeq \left.\frac{\partial^2 \phi_m}{\partial z^2}\right|_{z=z_b} - \left.\frac{\partial \phi_m}{\partial z}\right/Z_b\Big|_{z=z_b}. \tag{2}$$

At the bottom, we parameterize the scattering amplitude by a local scatterer distribution η, which is a function of range and azimuth and which, for the purposes of this development, is real and distributed Gaussian in amplitude[1]. From this scatterer the propagation back to the receiver is given by the Green's function

$$p_r(\omega, z_r, r) \simeq \sqrt{\frac{2\pi}{r}} \sum_{n=1}^{N} \frac{\phi_n(z_r)\phi_n^+}{\sqrt{k_n}} e^{ik_n r}, \tag{3}$$

where ϕ^+ represents the ability of the scatterer to excite the waveguide in the backscattered direction. Taken together, the backscattered field from scatterers

---

[1]To accommodate propagation uncertainty, it might be attractive in the future to model this as two independent Gaussian random variables, one for the in-phase component and one for the quadrature. However, the exact form of the distribution is only important for the determination of the higher moments of the short time average of the reverberation. The determination of these values will be the subject of a subsequent report.

at all ranges and azimuths at frequency ω is

$$p(\omega, z_s, z_r) = 2\pi \int_0^{2\pi} d\theta \int_0^\infty dr \sum_{m=1}^{N} \sum_{n=1}^{N} \phi_m(z_s)\phi_m^-\eta(r,\theta)\phi_n^+\phi_n(z_r)\frac{e^{i(k_n+k_m)r}}{\sqrt{k_n k_m}}. \quad (4)$$

The backscattered time series is then given by the inverse Fourier transform

$$
\begin{aligned}
p(t, z_s, z_r) &= \int_0^{2\pi} d\theta \int_0^\infty dr\, \eta(r,\theta) \\
&\times \int_{-\infty}^\infty d\omega A(\omega) \sum_{m=1}^{N}\sum_{n=1}^{N} \phi_m(z_s)\phi_m^-\phi_n^+\phi_n(z_r)\frac{e^{-i(\omega t-(k_n+k_m)r)}}{\sqrt{k_n k_m}}, \quad (5)
\end{aligned}
$$

where the mode shape functions $\phi_{n,m}$, the scattering functions $\phi_{n,m}^\pm$ and the modal eigenvalues $k_{n,m}$ are all implicit functions of frequency. Although such an expression can be evaluated numerically, solutions in this form cannot provide significant insight into the controlling characteristics of reverberation. Instead what is required is the short time average (STA) of the square of the quantity $p(t)$, since we are interested in intensity, and since we are interested in the expected intensity, we seek the ensemble average $\langle p_{STA}^2 \rangle$. In order to gain insight, we would also like to be able to evaluate the desired quantities analytically. Looking at Eq. (5), it seems that the two largest hurdles to closed form evaluation are the generally unknown spatial characteristics of the scatterer distribution η, and the frequency integrals over the modal Green's functions p_i and p_r. The first difficulty can be overcome if we assume that the spatially statistics of the scatterers are known. The second difficulty may be overcome for signals of limited bandwidth by making use of the narrowband approximation.

In the narrowband approximation, temporal responses of filters are approximated by expanding the filter response about a center frequency. In this application the filters of interest are the Green's functions in Eqs. (1) and (3). The mode shape functions and the scattering functions ϕ^+ and ϕ^- are both assumed to remain unchanged in the vicinity of the center frequency; the wavenumbers $k_{n,m}$ are assumed to change following the second order Taylor series expansion about the center frequency

$$k_n = k_n^o + (\omega - \omega_o)\frac{\partial k_n}{\partial \omega}\bigg|_{\omega=\omega_o} + \frac{(\omega-\omega_o)^2}{2}\frac{\partial^2 k_n}{\partial \omega^2}\bigg|_{\omega=\omega_o}. \quad (6)$$

Insertion of Eq. (6) into Eq. (5) and integrating over a bandwidth of $\triangle\omega$ yields the approximation

$$
\begin{aligned}
p(t, z_s, z_r) &= A(\omega_o)\Re\Bigg\{\int_0^{2\pi} d\theta \int_0^\infty dr\, \eta(r,\theta)\sum_{m=1}^{N}\sum_{n=1}^{N}\frac{\phi_m^o(z_s)\phi_m^{o-}\phi_n^{o+}\phi_n^o(z_r)}{\sqrt{k_n^o k_m^o}} \quad (7) \\
&\times\; e^{-i(\omega_o t-(k_n^o+k_m^o)r)}\int_{-\triangle\omega}^{\triangle\omega} d\omega e^{-i\omega(t-(S_{nm}+\frac{\omega}{2}D_{nm})r)}\Bigg\},
\end{aligned}
$$

where S_{nm} is the sum of the modal slownesses $\frac{\partial k_n}{\partial \omega} + \frac{\partial k_m}{\partial \omega}$, and D_{nm} is the sum of the modal dispersion terms $\frac{\partial^2 k_n}{\partial \omega^2} + \frac{\partial^2 k_m}{\partial \omega^2}$. If we assume for the moment that the modal dispersion is negligible, then the frequency integral in Eq. (8) may be performed with the result after some rearrangement

$$
\begin{aligned}
p(t, z_s, z_r) \; = \; & 2 \triangle \omega A(\omega_o) \Re \left\{ e^{-i\omega_o t} \sum_{m=1}^{N} \sum_{n=1}^{N} \frac{\phi_m^o(z_s) \phi_m^{o-} \phi_n^{o+} \phi_n^o(z_r)}{\sqrt{k_n^o k_m^o}} \right. \\
& \left. \times \int_0^{2\pi} d\theta \int_0^{\infty} dr \; \eta(r, \theta) e^{i(k_n^o + k_m^o)r} sinc(\triangle \omega(t - S_{nm} r)) \right\}.
\end{aligned}
\tag{8}
$$

Several intuitive observations may be made upon inspection of Eq. (8). The first is that the amplitude of the reverberation time series increases linearly with the bandwidth $\triangle \omega$, consistent with the fact that the energy in the time series is increasing as more frequencies are included. The second is that the contribution to the scattered field at time t comes from a region concentrated about $r = t/S_{nm}$, i.e. from ranges close to the time over the round trip modal slowness, a result which we observed at the beginning of this section derives directly from the narrowband approximation, which expands the kernel in the same way as a stationary phase evaluation of the inverse Fourier transform. Furthermore, we see that the response at time t is a local Fourier transform of the scattering process η, which is windowed by a *sinc* function whose spatial extent is approximately $\triangle r \simeq \frac{2\pi}{\triangle \omega S_{nm}}$ or approximately $c/2 \triangle f$, the classic "patch size" from reverberation analysis.

At this point it is useful to consider the different behavior of the reverberation in the limits of narrow and broadband frequency excitation. First there are the effects which exist in general for any particular mode pair and are not related to the coherent nature of the propagation which can introduce structure when Eq. (8) is summing coherently. If the spatial window is very narrow in extent (*i.e.* broadband excitation,) then the individual scatterers dominate the return at any given time and the spatial Fourier transform has inadequate aperture to allow resonant scattering to occur. In addition, we can expect the variance of the backscattered time series to be on the order of the variance of the individual scattering cross sections of the scatterers themselves, since very few scatterers contribute to the total return from each mode pair at any given time. On the other hand, if the spatial window is very broad, as is the case for very narrowband scattering processes, then the window is much larger than the correlation length scale of the individual scatterers and resonant scattering can occur. In this case, we can expect much lower amplitudes of backscatter compared to the level of individual scattering cross sections in the window, and lower overall variance of the reverberation intensity, since many correlation lengths of the scatterers are insonified.

The second effect of bandwidth is how it controls the amplitude of the interference terms between the modes. Since the individual modes have different slownesses,

we may expect coherent interference terms to disappear between modes where the difference between the range integrated round trip slowness $\Delta t_{nm} = (S_{nn} - S_{mm})r$ is greater than one over the bandwidth, *i.e.* $\Delta t_{nm} > 2\pi/\Delta\omega$. Put another way, modes which interrogate different patches of the bottom at a given time are decorrelated and will yield no interference structure associated with coherent propagation to the backscattered field. Thus for broad band excitation, we can expect significant variance in the reverberation intensity, but a fairly smooth mean; conversely, we expect highly structured mean reverberation intensity for narrow band excitation but lower variance about this structure. We can therefore anticipate that reverberation deviation from smooth parameterized curves comes from a combination of effects induced by propagation (waveguide effects) and effects introduced by the scatterers themselves.

Even though we can understand how the various terms in Eq. (8) control the character of the reverberation as a function of time, evaluation of the windowed Fourier transform of the spatial distribution of scatterers is difficult to quantify in closed form. For this reason we adopt a slightly different form of the narrow band approximation where now we assume that the bandwidth is controlled not by absolute frequency limits but by a Gaussian window function

$$A(\omega) = Ae^{-(\omega-\omega_o)^2/\Delta\omega^2},$$

which when inserted into Eq. (5) along with Eq. (6) yields a slightly different form of the narrowband approximation which will prove more useful

$$
\begin{aligned}
p(t, z_s, z_r) &= \sqrt{\pi}A\Re\left\{ e^{-i\omega_o t} \sum_{m=1}^{N}\sum_{n=1}^{N} \sigma_{nm} \frac{\phi_m^o(z_s)\phi_m^{o-}\phi_n^{o+}\phi_n^o(z_r)}{\sqrt{k_n^o k_m^o}} \right. \\
&\quad \left. \times \int_0^{2\pi} d\theta \int_0^\infty dr\, \eta(r,\theta)e^{i(k_n^o+k_m^o)r}e^{-(t-S_{nm}r)^2/4\sigma_{nm}^2} \right\},
\end{aligned} \tag{9}
$$

where $\sigma_{nm}^2 \equiv \Delta\omega^{-2} - iD_{nm}r/2$. The term $\exp(-(t-S_{nm}r)^2/4\sigma_{nm}^2)$ in Eq. (9) serves the same purpose as the *sinc* function in Eq. (8), with the added attraction that the dispersion D_{nm} is now included explicitly and that the windowed Fourier transform will be easier to evaluate in subsequent manipulations. However, all of the intuition we have gained concerning the effects of bandwidth remains valid, with an additional point which can be added concerning the effect of dispersion. Dispersion will have the effect of increasing the patch sizes at late times, both decreasing the variance of the scatterer contribution and increasing the importance of coherent propagation effects.

We now turn our attention to the short time average of Eq. (9). First we review complex envelope theory. Equation (9) has the form

$$p(t) = \Re\left\{ e^{-i\omega_o t}A(t) \right\},$$

where $A(t)$ is the so called complex envelope which is everything in the bracket in Eq. (9) following the $e^{-i\omega_o t}$. Squaring $p(t)$ and expanding we get

$$
\begin{aligned}
p^2(t) \;=\;& \Re\{A(t)\}^2 \cos^2(\omega_o t) + \Im\{A(t)\}^2 \sin^2(\omega_o t) \\
&+\; 2\Re\{A(t)\} \cos(\omega_o t)\Im\{A(t)\} \sin(\omega_o t)
\end{aligned}
$$

which upon a short time average yields

$$
\begin{aligned}
p^2_{STA}(t) \;\simeq\;& \frac{\Re\{A(t)\}^2}{2} + \frac{\Im\{A(t)\}^2}{2} \\
=\;& \frac{|A(t)|^2}{2} \\
=\;& \frac{A(t)A^*(t)}{2}.
\end{aligned}
\tag{10}
$$

Under the last identity, the short time average of the backscattered intensity, *i.e.* the square of Eq. (9), is given by

$$
\begin{aligned}
p^2_{STA}(t, z_s, z_1, z_2) \;=\;& \frac{\pi A^2}{2} \sum_{m=1}^{N} \sum_{n=1}^{N} \sum_{m'=1}^{N} \sum_{n'=1}^{N} \sigma_{nm}\sigma^*_{n'm'} \\
\times\;& \frac{\phi_m(z_s)\phi_{m'}(z_s)\phi^-_m\phi^-_{m'}\phi^+_n\phi^+_{n'}\phi_n(z_1)\phi_{n'}(z_2)}{\sqrt{k_n k_m k^*_{n'} k^*_{m'}}} \\
\times\;& \int_0^{2\pi} d\theta \int_0^{2\pi} d\theta' \int_0^{\infty} dr \int_0^{\infty} dr'\, \eta(r,\theta)\eta(r',\theta') \\
\times\;& e^{i(k_n+k_m)r}e^{-i(k^*_{n'}+k^*_{m'})r'}e^{-(t-S_{nm}r)^2/4\sigma^2_{nm}}e^{-(t-S_{nm}r')^2/4(\sigma^*_{n'm'})^2},
\end{aligned}
\tag{11}
$$

where k^* indicates $\Re\{k\} - i\Im\{k\}$ and the superscripts o indicating that the mode functions and eigenvalues are evaluated at the center frequency have been dropped for compactness of notation. Note that Eq. (11) gives the short time average of the reverberation intensity explicitly in terms of two receiver depths z_1 and z_2. Thus it is important to note that this development will yield the quantities necessary to predict the time dependent vertical coherence

$$
\rho^2(t, z_1, z_2) \equiv \frac{p^2_{STA}(t, z_1, z_2)}{\sqrt{p^2_{STA}(t, z_1, z_1)p^2_{STA}(t, z_2, z_2)}}.
\tag{12}
$$

Since sonar system operators in general have at most only general statistical characterizations of the bottom scattering parameters at their disposal, we will turn our attention to the evaluation of the ensemble average of Eq. (11). The only random variables in Eq. (11) are the scatterer distributions η. The ensemble average of these two distributions in Cartesian coordinates and under assumptions of spatial homogeneity is

$$
\langle\eta(r,\theta)\eta(r',\theta')\rangle \equiv R_\eta(r\cos\theta - r'\cos\theta', r\sin\theta - r'\sin\theta').
$$

If we assume that the scatterer autocorrelation function R_η corresponds to an anisotropic Gaussian parameterization with correlation length scales ℓ_x and ℓ_y and a skew angle aligned with $\theta \equiv 0$,

$$R_\eta = \frac{\langle \eta^2 \rangle}{2\pi \ell_x \ell_y} \exp(-(x^2/2\ell_x^2 + y^2/2\ell_y^2)), \tag{13}$$

and perform the change of variables $r'' = r' - r$ and $\theta'' = \theta' - \theta$, we have in the far field

$$x \simeq r'' \cos\theta - r\theta'' \sin\theta$$
$$y \simeq -r'' \sin\theta - r\theta'' \cos\theta. \tag{14}$$

Insertion of Eqs. (14) into Eq. (13) and integration over θ'' yields (See Annex A for details of the derivation)

$$\int_{-\theta}^{2\pi-\theta} d\theta'' R_\eta(r, r'', \theta, \theta'') \simeq \frac{\langle \eta^2 \rangle}{\pi r \ell_y \sqrt{2\pi(\sin^2\theta + \ell_x^2/\ell_y^2 \cos^2\theta)}}$$
$$\times \exp(\frac{r''^2}{\ell_x^2/2} \frac{(\ell_x^2/\ell_y^2 - 1)^2}{\sec^2\theta + \ell_x^2/\ell_y^2 \csc^2\theta})$$
$$\times \exp(-r''^2(\frac{\cos^2\theta}{2\ell_x^2} + \frac{\sin^2\theta}{2\ell_y^2})), \tag{15}$$

which delivers the commonly adopted r^{-1} term heretofore missing from the reverberation equations. The result shows that the geometric decay in the reverberation level is due solely to the azimuthal decorrelation of the scattering centers. This term can only be obtained explicitly upon seeking the ensemble average, and is not explicitly present in Eq. (11), which on first inspection might seem to indicate that the reverberation intensity does not decay with increasing time. Of course realizations of the short time average will show this decay for all times associated with reverberation coming from ranges significantly greater than a correlation length scale, as the double azimuthal integral will introduce a linearly decreasing number of correlated components for increasing range.

In the limit of isotropic roughness with correlation length l, the ensemble average of the short time average of the reverberation intensity reduces to

$$\langle p_{STA}^2(t, z_s, z_1, z_2) \rangle = 2\pi^2 A^2 \sum_{m=1}^{N} \sum_{n=1}^{N} \sum_{m'=1}^{N} \sum_{n'=1}^{N} \frac{\langle \eta^2 \rangle}{r l \sqrt{2\pi} \sqrt{\sigma_{nm}^2 \sigma_{n'm'}^2}}$$
$$\times \frac{\phi_m(z_s)\phi_{m'}(z_s)\phi_m^- \phi_{m'}^- \phi_n^+ \phi_{n'}^+ \phi_n(z_1)\phi_{n'}(z_2)}{\sqrt{k_n k_m k_{n'}^* k_{m'}^*}}$$
$$\times \int_0^\infty dr \int_{-r}^\infty dr'' e^{-r''^2/2l^2} e^{i(k_n+k_m-(k_{n'}+k_{m'}))r} e^{-i(k_{n'}^*+k_{m'}^*)r''}$$
$$\times e^{-(t-S_{nm}r)^2/4\sigma_{nm}^2} e^{-(t-S_{n'm'}(r+r''))^2/4(\sigma_{n'm'}^*)^2}.$$

If we approximate r^{-1} in the kernel by S_{nm}/t and evaluate σ_{nm}^2 approximately as $\triangle\omega^{-2} - iD_{nm}t/2S_{nm}$ then all the remaining range dependence of the kernels resides in linear and quadratic terms in the arguments to the exponentials. If we take the further approximation of taking the lower limits on the range integrals as $-\infty$, the two range integrals may be evaluated exactly (see Annex B for details.) Under these approximations the ensemble average of the short time average of the reverberation intensity is

$$\langle p_{STA}^2(t, z_s, z_1, z_2)\rangle = 2\pi^2 A^2 \sum_{m=1}^{N}\sum_{n=1}^{N}\sum_{m'=1}^{N}\sum_{n'=1}^{N} \frac{\langle\eta^2\rangle S_{nm}}{t\ell\sqrt{2\pi}\sqrt{\sigma_{nm}^2\sigma_{n'm'}^2}}$$

$$\times \frac{\phi_m(z_s)\phi_{m'}(z_s)\phi_m^-\phi_{m'}^-\phi_n^+\phi_{n'}^+\phi_n(z_1)\phi_{n'}(z_2)}{\sqrt{k_n k_m k_{n'} k_{m'}}}$$

$$\times \exp\left\{\left(t\left(\frac{S_{n'm'}}{2\sigma_{n'm'}^2}(R-1) - \frac{S_{nm}}{2\sigma_{nm}^2}\right) - i(k_n + k_m - (k_{n'} + k_{m'})(1-R))\right)^2\right.$$

$$\left.\times \left(\frac{S_{nm}^2}{\sigma_{nm}^2} + \frac{S_{n'm'}^2}{\sigma_{n'm'}^2}(1-R)\right)^{-1}\right\}$$

$$\times \exp\left\{-\left(t^2\left(\frac{1}{4\sigma_{nm}^2} + \frac{1-R}{4\sigma_{n'm'}^2}\right) + it\frac{k_{n'}+k_{m'}}{S_{n'm'}}R + \frac{(k_{n'}+k_{m'})^2\sigma_{n'm'}^2}{S_{n'm'}^2}R\right)\right\}$$

$$\times \sqrt{\pi\left(\frac{S_{n'm'}^2}{4\sigma_{n'm'}^2} + 1/2\ell^2\right)^{-1}}\sqrt{\pi\left(\frac{S_{nm}^2}{4\sigma_{nm}^2} + \frac{S_{n'm'}^2}{4\sigma_{n'm'}^2}(1-R)\right)^{-1}} \quad (16)$$

where

$$R = \left(1 + 2\sigma_{n'm'}^2/S_{n'm'}^2\ell^2\right)^{-1}. \quad (17)$$

In Eq. (16) and (17) all quantities with primed subscripts are assumed to be conjugated.

Equation (16) gives the ensemble average of the short time average of the reverberation intensity directly in terms of time, modal slownesses, modal dispersion and the correlation length scale of the scattering process. The arguments to the exponential functions all sum to a number smaller than zero. This is intuitive since the exponential functions indicate the contributions to the reverberation between mode sets. For this reason the product of the exponential functions may be viewed as a time dependent modal correlation function ρ^2.

In order to gain insight into the expected behavior of the reverberation intensity, it is useful to evaluate the behavior of the modal correlation function in simplified circumstances. In the limit of zero dispersion, ρ^2 may be written

$$\rho^2_{nmn'm'}(t,\ell,\triangle\omega) \rightarrow \exp\left\{\frac{\left(\frac{t\triangle\omega}{2}\left(S_{nm}+\frac{S_{n'm'}}{1+\ell^2/2L^2}\right)+\frac{i}{\triangle\omega}\left(k_n+k_m-\frac{k_{n'}+k_{m'}}{1+\ell^2/2L^2}\right)\right)^2}{S^2_{nm}+S^2_{n'm'}/(1+\ell^2/2L^2)}\right\}$$

$$\times \exp\left\{-\left(\frac{t^2\triangle\omega^2}{4}\left(\frac{2+\ell^2/2L^2}{1+\ell^2/2L^2}\right)+i\frac{t(k_{n'}+k_{m'})}{S_{n'm'}(1+2L^2/\ell^2)}\right.\right.$$

$$\left.\left.+\frac{(k_{n'}+k_{m'})^2\ell^2}{2+\ell^2/L^2}\right)\right\}$$

$$\times \sqrt{\pi(1/4L^2+1/2\ell^2)^{-1}}\sqrt{\pi\left(\frac{S^2_{nm}\triangle\omega^2}{4}+\frac{S^2_{n'm'}\triangle\omega^2}{4+2\ell^2/L^2}\right)^{-1}} \quad (18)$$

where L is the patch size $1/\triangle\omega S_{n'm'}$.

It is instructive to evaluate Eq. (18) in the limits of patch size large and small in relation to the correlation length scale. In the large patch size limit ($L \gg \ell$) we obtain for the intermodal correlation function (see Annex C for the details of the derivation)

$$\rho^2_{nmn'm'}(t, L \gg \ell) \simeq e^{-(k_n+k_m-(k_{n'}+k_{m'}))^2L^2/2}$$

$$\times e^{-(k_{n'}+k_{m'})^2\ell^2/2}$$

$$\times e^{it\frac{k_n+k_m-(k_{n'}+k_{m'})}{S_{nm}}}$$

$$\times e^{-t^2(S^{-2}_{nm}+2S^{-1}_{nm}S^{-1}_{n'm'}+S^2_{n'm'})/8L^2}. \quad (19)$$

The first term of Eq. (19) represents a decorrelation between modes due to very large patch size and differences between the modal wavenumbers which causes a cancellation phenomenon. The second term represents the traditional Bragg scattering term, which is the Fourier transform of the correlation function R_η at the sum of the incident and scattered wavenumbers. The argument to the third term is the difference between the round trip phase between the various candidate mode sets in the modal sum. This is identical to the magnitude square of the modal interference terms in the round trip propagation to the scattering patch and back, and so represents a coherent propagation effect. The fourth term is a spatial decorrelation term which increases with range. This represents the decorrelation between modes due to the fact that different physical parts of the bottom are illuminated by the two round trip mode sets. The equivalent form is

$$e^{-t^2\triangle r^2/8L^2},$$

where $\triangle r$ represents the range separation between the patches associated with each mode set. For broadband processes we next show that this decorrelation is controlled by the correlation length scale ℓ instead.

Equation (19) represents the traditional view of scattering in the narrow band limit; where the patch size is sufficient to allow Bragg type scattering to occur and lower backscattered levels are achieved. The first term in Eq. (19) also limits the amount of interference structure allowed between mode sets, and in the limit of infinitesimal bandwidth ($L \to \infty$) decorrelates all the modal cross terms, destroying the propagation structure. This transition is given explicitly in the waveguide and bandwidth parameters.

In the small patch size limit ($\ell \gg L$) Eq. (18) reduces to (see Annex C)

$$\rho^2_{nmn'm'}(t, \ell \gg L) \simeq e^{-((k_n+k_m)^2+(k_{n'}+k_{m'})^2)L^2}$$
$$\times \; e^{it(\frac{k_n+k_m}{S_{nm}}-\frac{k_{n'}+k_{m'}}{S_{n'm'}})}$$
$$\times \; e^{-t^2(S_{nm}^{-2}-2S_{nm}^{-1}S_{n'm'}^{-1}+S_{n'm'}^{-2})/2\ell^2}, \qquad (20)$$

where the last term is equivalent to

$$e^{-\Delta r^2/2\ell^2},$$

and represents a decorrelation between mode sets associated with the ratio between the distance between the mode patches Δr and the correlation length scale ℓ.

The first term in Eq. (20) represents decorrelation between mode sets associated with the spatial aperture L, and differs from the analogous term in Eq. (19) in that this decorrelation remains finite for even the diagonal terms where the mode sets are identical. In fact this term bears more of a resemblance to the Bragg scattering term from the second line of Eq. (19), and may be thought to replace it with a term of approximately the form
$$e^{-(k_{n'}+k_{m'})^2 2/L^2}.$$

This is a key result which shows that in the limit of small patch size, Bragg scattering associated with the correlation function of the scattering centers disappears, and is replaced by a term which looks very much like Bragg scattering from a scattering process with the smaller spatial scale L. This is the manifestation of the extremely strong window effect present at short spatial window scales: the local Fourier transform of the spatial correlation function is severely distorted by the small spatial window, with the result that the amplitude of the backscattered field is determined more by the variance of the individual scatterers themselves than by resonant type terms obtained through the interrogation of multiple scatterers by the larger spatial windows obtained with narrower bandwidths.

The second term is the round trip accumulated phase as in Eq. (19), with the distinction that the phase accumulated on the return trip is integrated over the range $t/S_{n'm'}$ associated with the primed mode set. This distinction is thought to be inconsequential in comparison to the other differences noted above.

3

Results

In this section we use the theory developed in the last section to predict the short time average of reverberation intensity for the shallow water environment observed during the SCARAB'97 experiment in the Capraia basin north of Elba [3]. The purpose of this section is not to interpret the data from this experiment, but rather to use realistic parameters to show how the reverberation depends on the parameters of center frequency, bandwidth, scattering layer, and correlation length scale, as well as sourcer-receiver geometry.
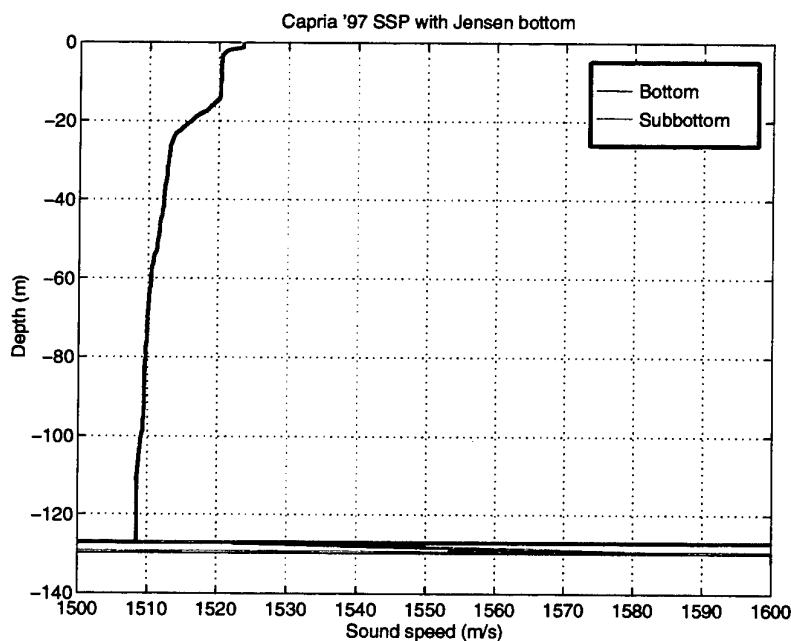
Figure 1 *The SCARAB '97 environment chosen for this study. This environment models summertime shallow water conditions in the Capraia basin north of Elba. The environment consists of a measured sound speed profile taken by XBT on top of an upwardly refracting sediment 2.5 m thick with a density of 1.75 g/cm^3 with a sound speed ranging from 1520 m/s at the water-sediment interface to 1580 m/s at the sediment-subbottom interface. The subbottom has a density of 1.8 g/cm^3 and has a 1600 m/s sound speed.*

Depth	Sound speed (m/s)	Density (g/cm^3)	Attenuation (dB/λ)
0	1520	1.75	0.13
2.5	1580	1.75	0.13
halfspace	1600	1.80	0.15

Table 1 *Capraia basin bottom properties used as input into KRAKEN for the calculation of modal properties.*

The SCARAB'97 experiment was conducted in June, so the measured sound speed profiles were downward refracting. The bottom properties in the Capraia basin have been the subject of considerable study [4, 5]; here we adopt a fast upwardly refracting bottom used by Jensen to adequately characterize the transmission loss [6]. The sound speed profile in the water column and into the bottom is illustrated in Fig. 1, and the bottom properties used are indicated in Table 1.
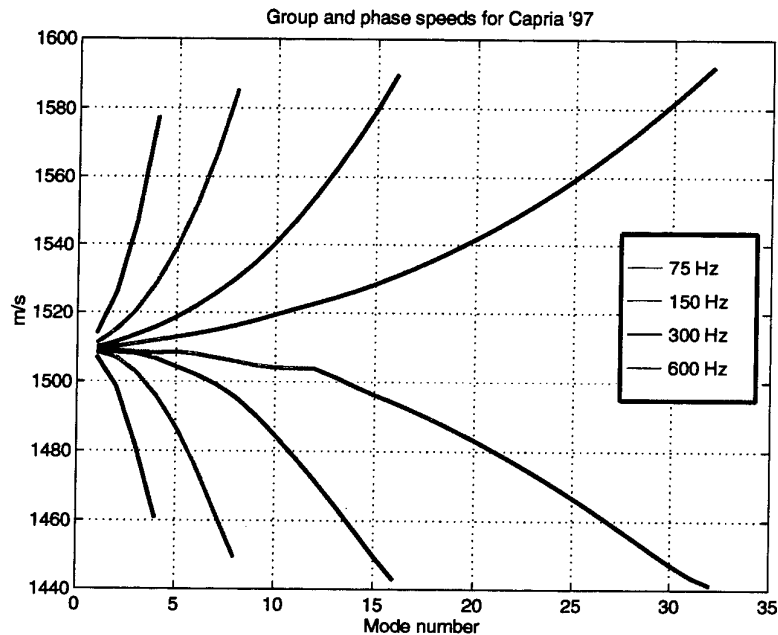
Figure 2 *The phase (upper curves) and group speed (lower curves) obtained for the environment in* **Fig. 1** *using KRAKEN. The repulsion of the phase and group speeds is typical of shallow water environments with significant boundary interactions. The feature in the group speed near mode 11 is associated with the penetration of the higher order modes into the 2.5 meter thick sediment.*

KRAKEN [7] was used to obtain the mode shape functions ϕ_n and the complex wavenumbers k_n for this waveguide at center frequencies of 75, 150, 300, and 600 Hz. The group slownesses $\partial k_n/\partial\omega$ and the modal dispersion $\partial^2 k_n/\partial\omega^2$ were deter-
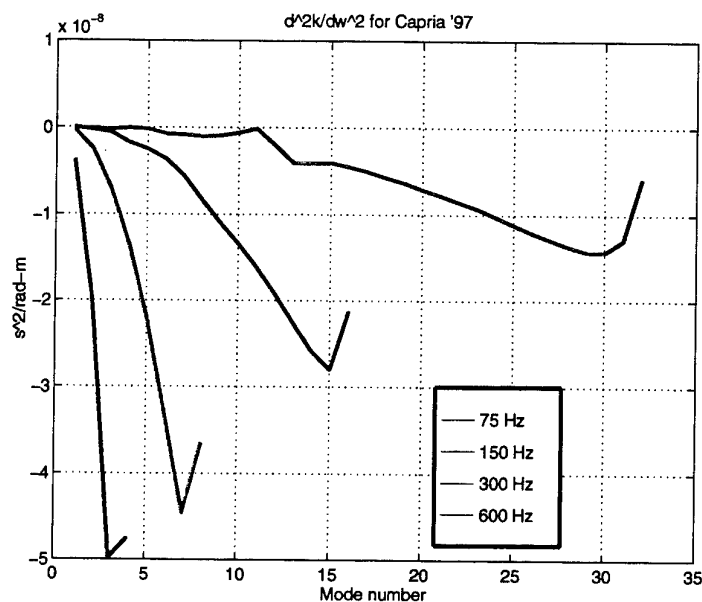
Figure 3 *The modal dispersion term $\partial^2 k_n/\partial\omega^2$ for the SCARAB'97 environment. These results, obtained by finite difference, indicate that individual modal arrivals spread out over time/range as the modes propagate. The negative sign on these values indicates that the lower frequencies have more slowness than high frequencies. Therefore in this environment high frequencies arrive first in individual modal arrivals.*

mined for these center frequencies by finite differences, using a 10 Hz step size. The resulting dispersion curves of the waveguide are indicated in Figs. 2 and 3. Inspection of the phase and group speeds of the modes shows that there is the typical low frequency shallow water behavior, with decreasing group speed for increasing mode number. Fig. 3 shows that the magnitude of the dispersion of the modes is in general increasing for increasing mode number, which means that higher order modes spread out more in time (and space) at long range than do lower order modes, and that the sign on the dispersion is negative, which indicates that the higher frequencies have less slowness, and therefore travel faster, than do the lower frequencies. The result is that at a given bottom patch, the highest frequencies for any given mode reach the patch first, and the modes themselves arrive in the order of increasing mode number. Close inspection of the dispersion curves indicates that there is an interesting kink in the group speed near mode number 11 at 600 Hz. This feature is associated with the penetration of the modes into the upwardly refracting sediment layer, and results in near zero modal dispersion for mode 11, a circumstance usually associated with lower order modes.
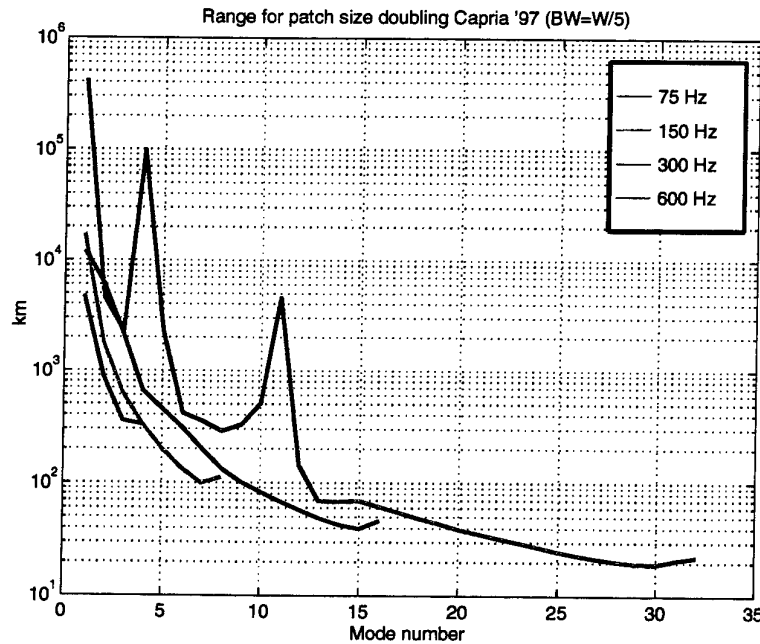
Figure 4 *The range at which the bottom patch illuminated by individual modes doubles in size as a function of frequency. For this result, 20% proportional bandwidth of the pulse is assumed. The results indicate that for lower order modes the patch size only doubles after 1000 km, while for higher order modes the patch size can double after as few as 20-40 km.*

The importance of including the modal dispersion term may be understood in terms of a range at which this term effectively decreases the bandwidth by a factor of two (with the effect of increasing the patch size and therefore the number of contributing scatterers at related times by a factor of two.) According to the definition of σ_{nm}^2, this range is given approximately by the relation $r_{2\Delta\omega} = 4/\Delta\omega^2\partial^2 k_n/\partial\omega^2$. At 600 Hz for 120 Hz of bandwidth, this range occurs at 30 km for mode 23. The range for patch size doubling is plotted in Fig. 4 for various center frequencies for the case where the bandwidth is equal to one fifth of the center frequency. As this range is proportional to the inverse square of the bandwidth, we see that the importance of including this term is accentuated for greater proportional bandwidths.

The transmission loss throughout the water column and into the first few meters of bottom is indicated for the four frequencies of interest in Fig. 5. The number of homogeneous modes with phase speed less than the subbottom speed of 1600 m/s ranges from 4 at 75 Hz to 32 at 600 Hz. The source depth was chosen in such a way as to emphasize coherent interaction between the modes. This is particularly evident at 150, 300 and 600 Hz, where the downward refracting nature of the waveguide becomes increasingly evident with frequency, yielding bundles of bottom interacting

rays with a 2 to 2.5 kilometer cycle distance. These strong bottom interactions will be seen to yield increased reverberation at the two-way travel time to the appropriate ranges.

The range-depth transmission loss, the transmission loss at the scattering interface, and the short time average of the reverberation received monostatically at 10 m depth are shown for the four frequencies of interest in Figs. 6 through 9. In almost all of these plots, the similarity between the one-way TL to the scatterers and the RL for a receiver depth of 75 m is apparent. The abscissas of the TL plots are scaled in such a way that the range maps directly to the average two way group speed of 750 m/s. Fig. 6 indicates no strong similarity between the RL and the TL plots at 75 Hz, but Fig. 7 shows that the strong bottom interaction at approximately 7 km at 150 Hz is seen to cause an associated large feature in the RL at $T \simeq (7000\text{m})/(750\text{m/s})$ or about 9 seconds. Two other strong bottom interactions at approximately 13 and 14.5 km also are seen to cause strong reverberation features at the appropriate travel time.

In Fig. 8 the increasingly ray-like propagation shows an increased number of local strong bottom interactions in the TL; two of these in particular show up in the RL, from ranges of 6 and 12 km. In Fig. 9 the 600 Hz results show that the theory predicts strong reverberation features at 7.5, 14 and 17.5 seconds, consistent with regions of strong bottom illumination in the TL at ranges of 6, 11 and 13 km.

These results represent an overview of the types of results which can be obtained with the theory. They were obtained with a perturbation theory scattering kernel representation outlines in Annex D for rough surface scattering from the bottom. The characteristics of these scattering kernels for water-sediment and sediment-subbottom rough surface scattering is outlined in the following sub-section.
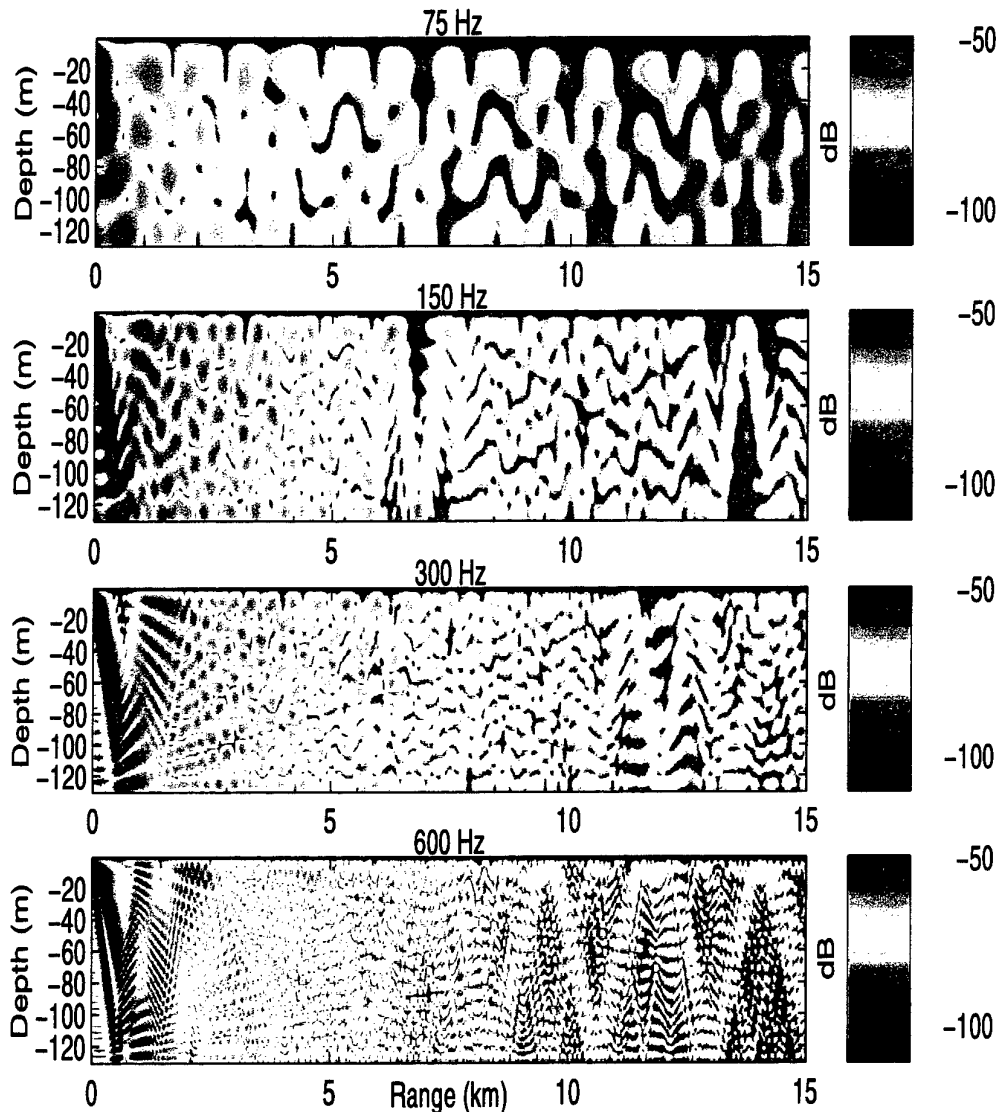
Figure 5 *The transmission loss throughout the watercolumn and into the first few m of bottom for the SCARAB'97 environment. Results are shown for 75, 150, 300 and 600 Hz. The source depth is 10 m and the receiver depth is 75 m. Results show that for 150 Hz and higher, the energy is organized into ray-like arrivals which interact strongly with the bottom at specific ranges. These strong coherent bottom interactions can cause strong features in the RL time series. The coherent reverberation model developed in this report captures these effects.*
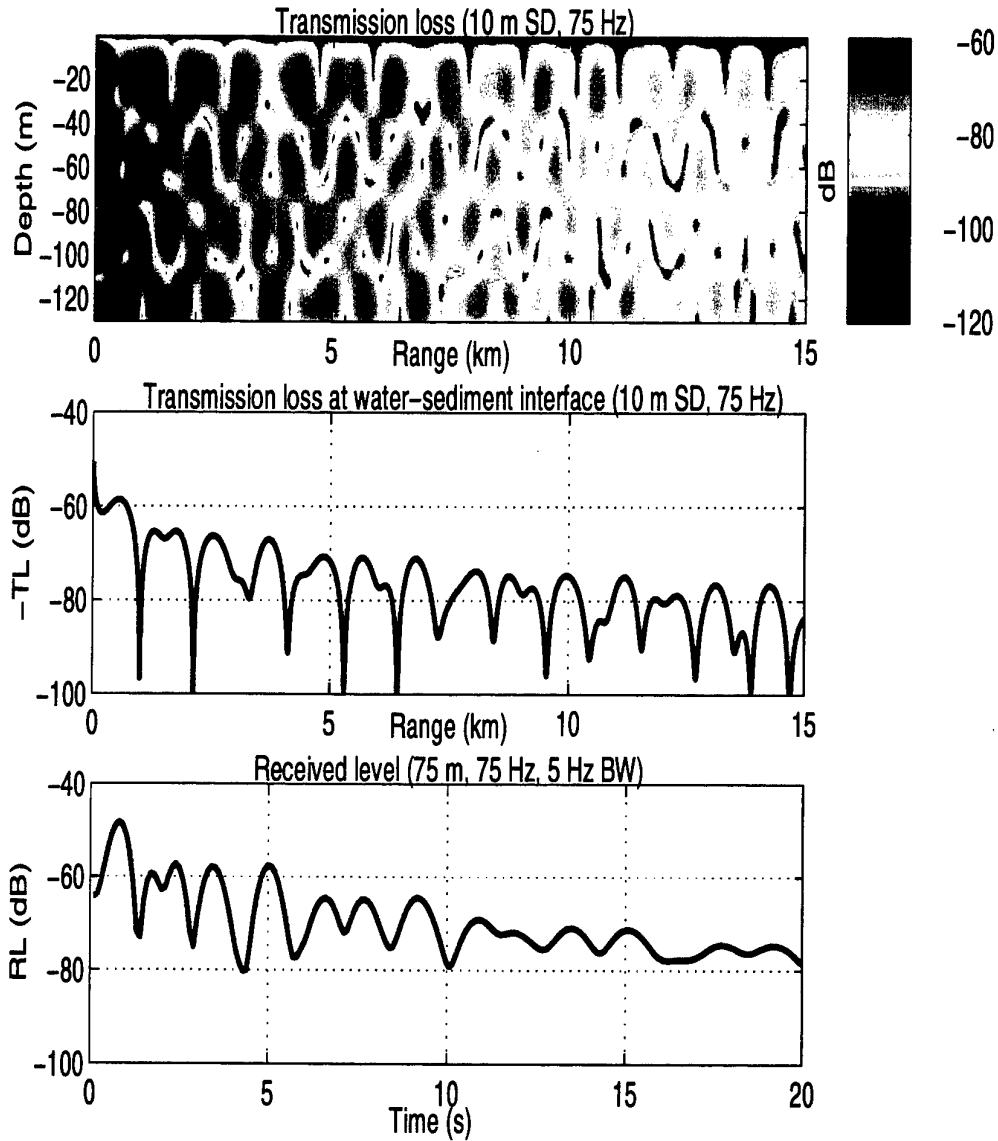
Figure 6 *A comparison between the TL and the RL for propagation and scattering in the SCARAB'97 environment at 75 Hz. The second plot is the one-way TL to the scattering interface. The third plot is the predicted RL for scattering from this interface caused by a 1 m rms roughness with a correlation length scale of 0.5 m. The result is obtained for a bandwidth of 5 Hz.*
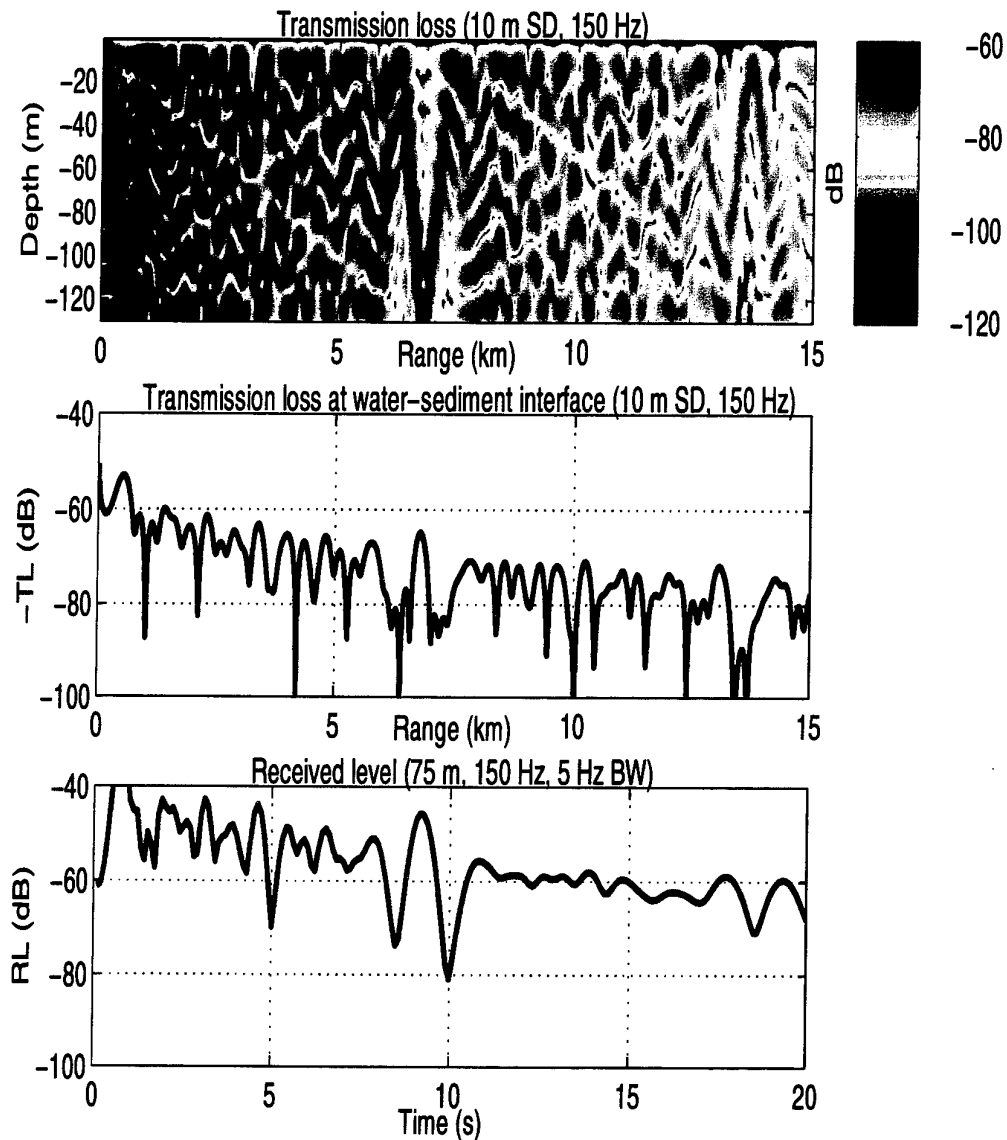
Figure 7 *This comparison between TL and RL at 150 Hz shows that the strong bottom interaction at 7 km causes an associated higher intensity return in the RL at about 9 seconds. The null in the TL at 14 km also shows up in the RL at the appropriate time of 18 seconds. In this figure the axis on the RL plot is equal to the range from the TL plots divided by a round trip group speed of 750 m/s. With this scaling strong features in RL can be directly associated on the abscissa with the propagation features which cause them.*
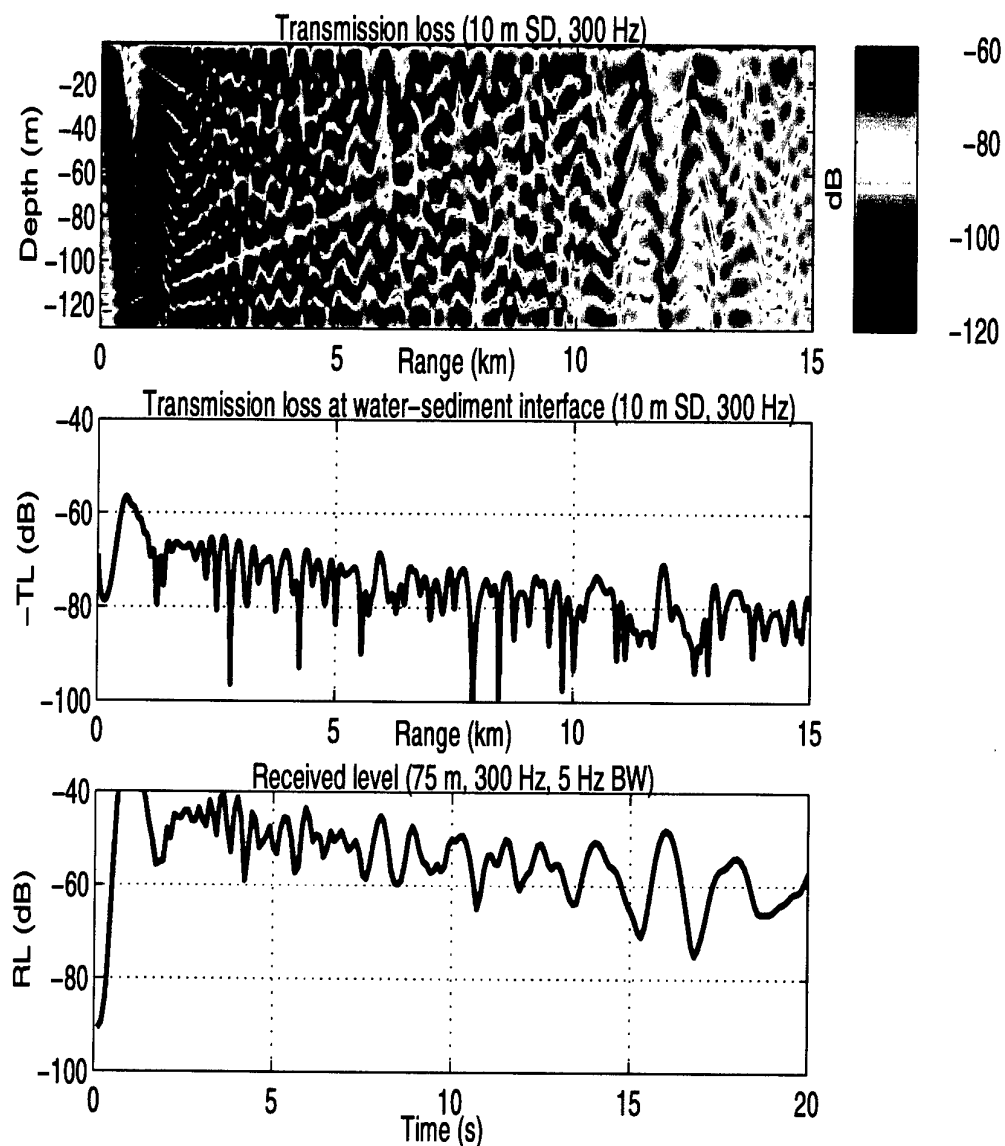
Figure 8 *At* 300 *Hz strong bottom interactions at 6, 10.5, 12 and 13.5 km cause associated spikes in the RL at 8, 14, 16 and 17.5 seconds. Again the scatterers are at the water-sediment interface with a correlation length scale of 0.5 m. The bandwidth is 5 Hz. The coherent interaction between modes for this relatively narrow bandwidth ensures that the underlying CW propagation structure leaves its imprint on the RL. For broader bandwidths, the structure at late time is reduced.*
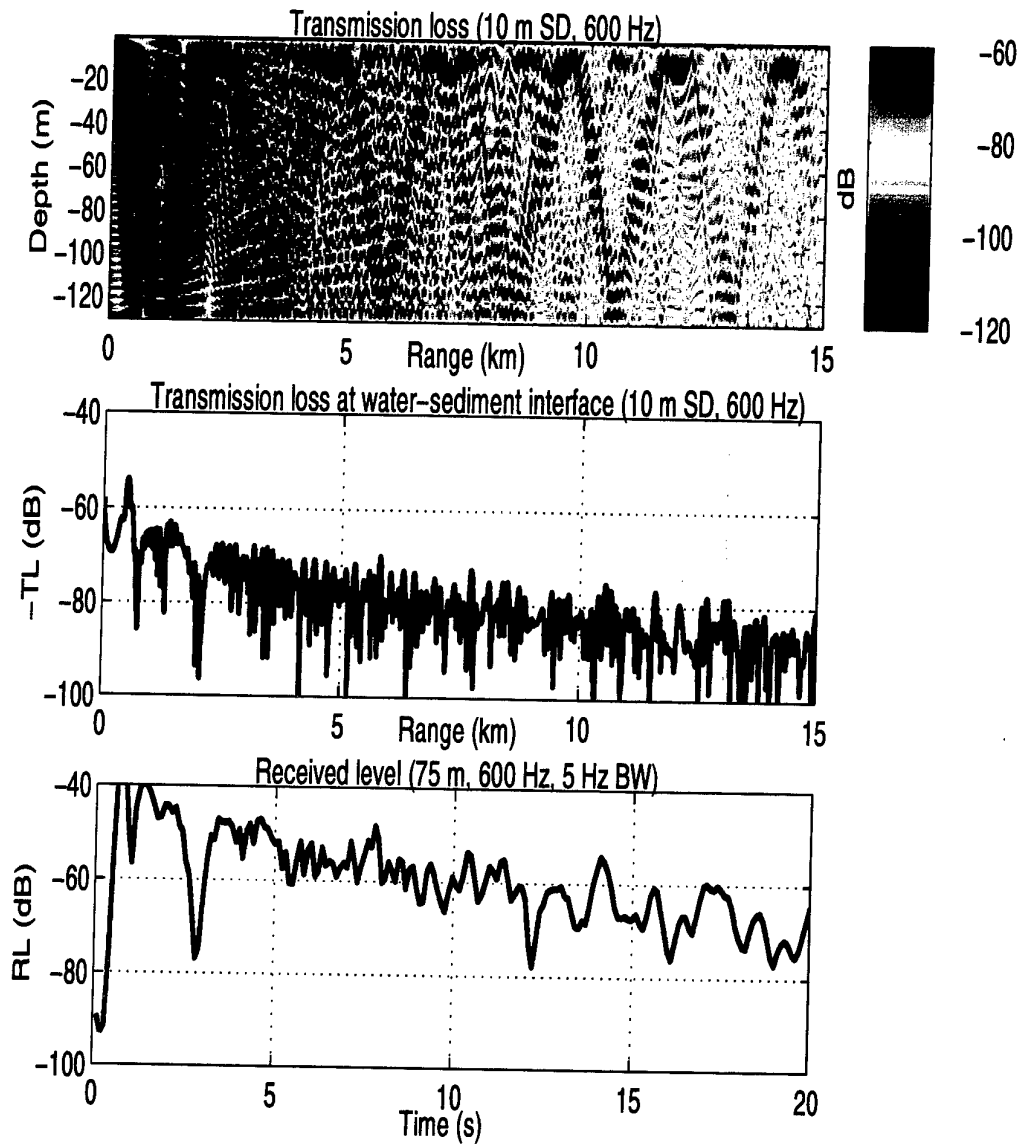
Figure 9 *At* 600 *Hz the TL structure begins to look strongly ray-like, with very strong local interactions at a variety of spatial locations. The bottom near 8, 10.5 and 13 km is particularly strongly illuminated by several ray bundles, causing associated features in the RL at 10, 14 and 17.5 seconds. A strong null in the TL at 2 km range also causes a strong dip in the RL at 3 seconds.*

3.1 Contributions from water-sediment and sediment-subbottom roughness

In this theory, three separate parameters together determine the importance of scattering into and out of the various modes. These parameters are 1) ϕ_n^-, the ability of the incident mode n to excite scattering, 2) ϕ_m^+, the ability of the scattered field to re-radiate into the scattered mode m, and 3) the modal attenuation associated with the complex modal eigenvalues $k_{n,m}$. In the simplified rough surface scattering theory developed in Annex D, the ability to excite rough surface scattering is determined by the difference between the second derivative of the mode shape function at the interface and the square of the first derivative normalized by the mode shape function at the scatterer depth

$$\phi_n^- \simeq \left(\frac{(\partial \phi_n/\partial z)^2}{\phi_n} - \frac{\partial^2 \phi_n}{\partial z^2} \right) \bigg|_{z=z_s}.$$
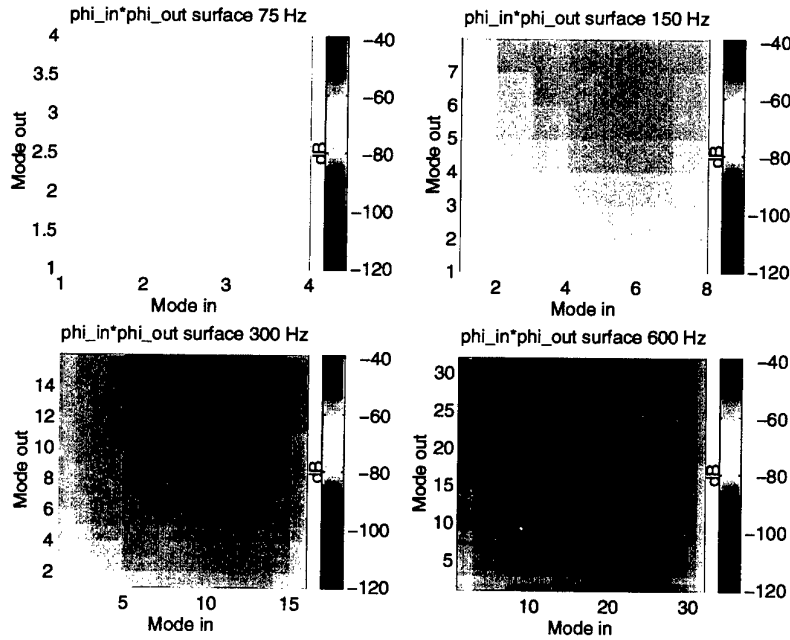

Figure 10 Scattering kernel *for rough surface scattering from the water-sediment interface. Lower order modes excite less scattering, and re-radiate less effectively. This kernel is obtained under a perturbation approximation, which for homogeneous boundary scattering would lead to the overall power of the kernels increasing 6 dB per octave. Here the increase is seen to be greater, mostly due to the increasing impedance contrast of the water-sediment interface at higher frequencies.*

In the simplified theory the ability of the scattered energy to re-radiate into modes is taken simply as the point source expansion into the backward propagating modes
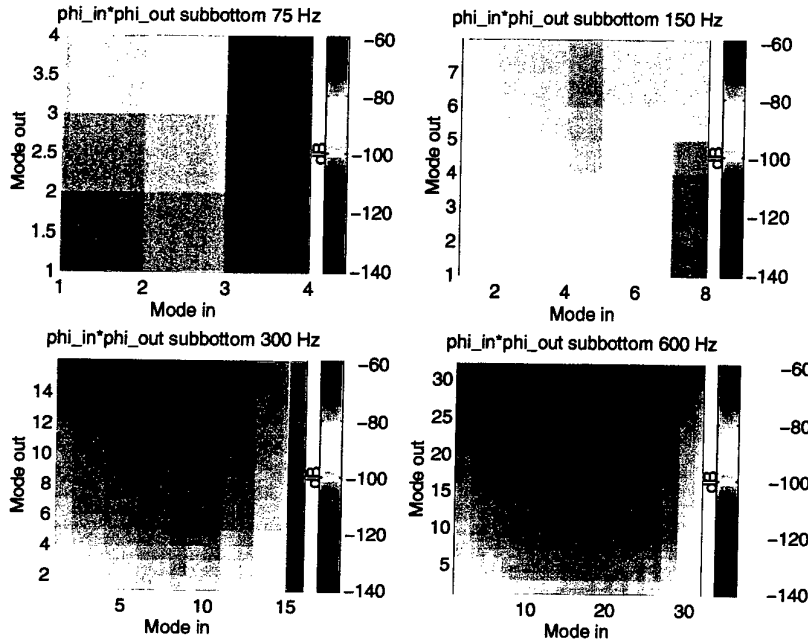
$$\phi_m^+ = \phi_m.$$

Figure 11 Scattering kernel *for sediment-subbottom rough interface scattering. These kernels have approximately 20 − 40 dB less power than the water-sediment interface kernels in* **Fig. 10** *due to the lower impedance contrast between the sediment and the subbottom. Near mode cut-off these scattering kernels become smaller because the sediment-subbottom interface impedance goes to zero, resulting in very little potential for scattering.*

Under these assumptions, the *scattering kernels* for rough surface scattering, which are magnitude square of the outer product of the scattering functions ϕ_n^- and ϕ_m^+, can be computed using the known mode shape functions. The results are illustrated in Fig. 10 for scattering from the water-sediment interface, and in Fig. 11 for scattering from the sediment-subbottom interface. These results show that in addition to about 20 − 40 dB less scattering potential from the sediment-subbottom scatterers, due to the lower impedance contrast, there is also a markedly different spectral characteristic to the response. For example, it can be seen that there is much lower scattering out of, and back into, the lower order modes, especially at 600 Hz. This is caused by the reduced interaction of the lower order modes with the sediment-subbottom interface due to the fast subbottom and the lower grazing angle of these modes.
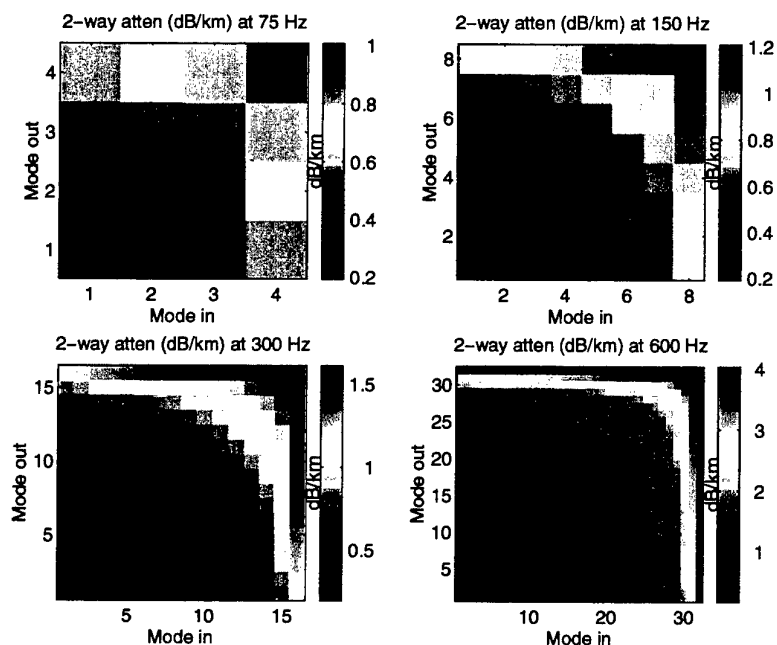
Figure 12 *The two way loss due to the bottom loss tangent for the SCARAB'97 environment. These values highlight the harshness of the shallow water environment for the propagation of acoustic energy. At 600 Hz the modes near cutoff are losing nearly 4 dB of acoustic energy for every additional kilometer of propagation to and from a scattering patch.*

As time increases, the third factor begins to assert its dominance over the angular characteristics of the backscatter. The modal attenuation, illustrated in dB per km in Fig. 12 for two way travel in the incoming and the backscattered mode pair, filters out the backscattering contribution from the higher order modes. Thus we can define an *effective scattering kernel*

$$\left| \phi_n^- e^{-R\Im\{k_n\}} e^{-R\Im\{k_m\}} \phi_m^+ \right|^2 ,$$

which is an explicit function of scatterer range R, may be calculated from the scattering functions ϕ_n^- and ϕ_m^+ and the complex modal eigenvalues. The results for sediment and subbottom interface scatterers at a scatterer range of 16 km are illustrated in Figs. 13 and 14 respectively. Comparison between Fig. 10-11 and 13-14 shows that the higher incident and scattered mode numbers contribute significantly less to the total scattering from a scatterer at 16 km than they do from a scatterer at short range.
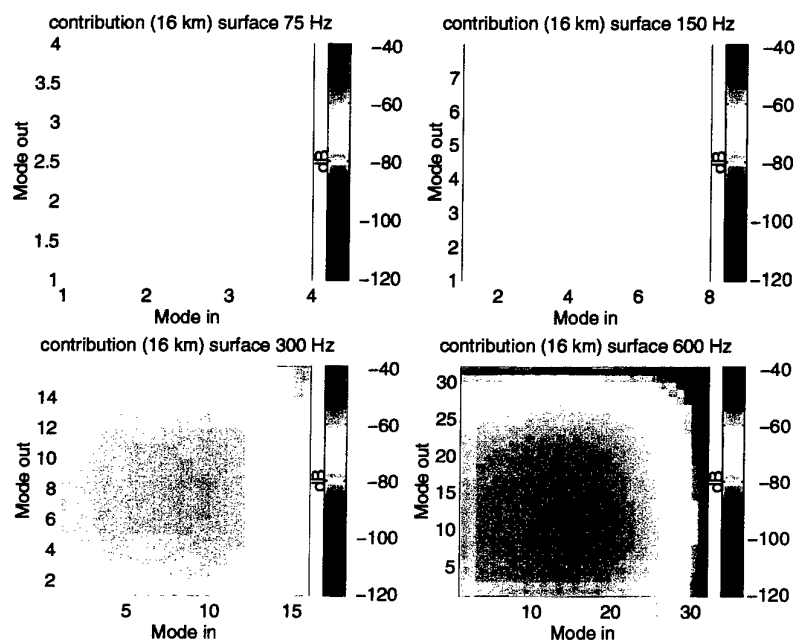
contribution (16 km) surface 75 Hz

contribution (16 km) surface 150 Hz

contribution (16 km) surface 300 Hz

contribution (16 km) surface 600 Hz

Figure 13 *The* effective scattering kernel *for scattering from water-sediment interface roughness 16 km from the source. The high attenuation for the higher order modes results in reduced contributions from these mode pairs. The result is that modes between the first third and half of the modal spectrum contribute the greatest amount to the RL.*
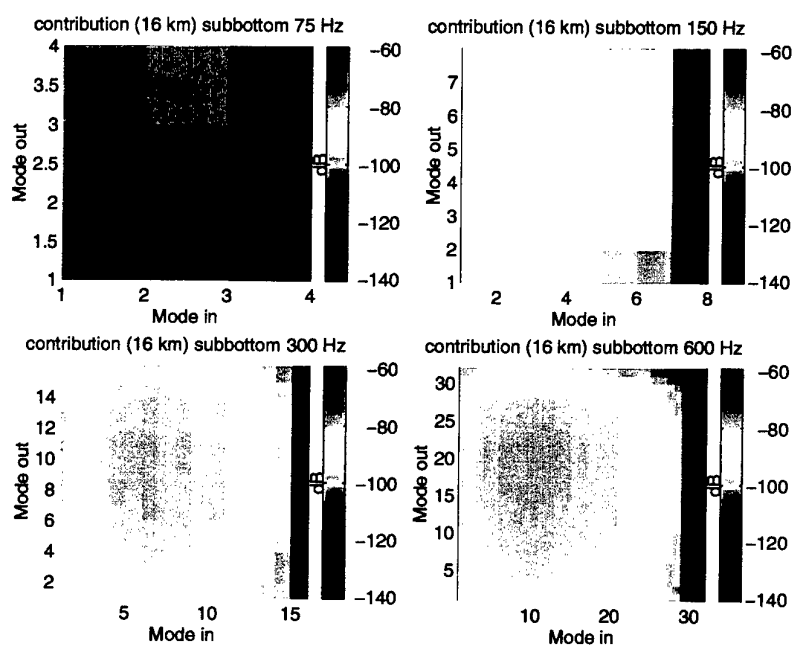
Figure 14 *The* effective scattering kernel *for scattering from sediment-subbottom interface roughness 16 km from the source. Incident mode numbers near the first third of the propagating modes, scattering into mode numbers near the midpoint of the propagating modal spectrum, give the greatest contribution to the RL for scatterers at this range.*

3.2 Effect of center frequency on RL

The center frequency controls the characteristics of the reverberation by changing the characteristics of the forward propagation and by changing the magnitude and shape of the scattering kernel. The ratio of the wavelength to the correlation length scale also has a very strong influence on the amplitude of the reverberation, especially for Gaussian scatterer spatial correlation properties. For perturbation theory of rough surface scattering outlined in Annex D, scattering from homogeneous boundaries is predicted to increase proportional to frequency squared. However, as frequency increases for a fixed correlation length scale, the Bragg scattering condition begins to reduce the component of energy backscattered to the receiver. The result is that for scatterers distributed according to a Gaussian correlation function, the theory predicts that there is a frequency of maximum backscattering.
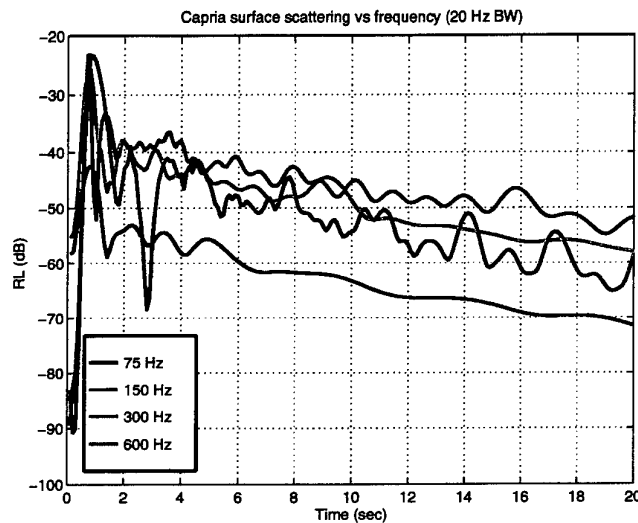

Figure 15 *The RL as a function of frequency for water-sediment interface rough-ness scattering from a roughness with a 0.5 m correlation length scale. Results are computed at 75, 150, 300 and 600 Hz assuming 20 Hz of bandwidth. The RL is predicted to have a maximum near 460 Hz due to correlation length scale effects. The results shown here indicate that maximum RL is obtained at 300 Hz, with approximately equal RL at 150 and 600 Hz.*

The frequency of maximum backscatter is that frequency above which, for sufficiently narrow bandwidths, resonant scattering effects would cause a rapid fall-off of the RL. For Gaussian correlated scatterers, this frequency has a magnitude of approximately $230/\ell$. At this frequency, the power of the resonant scattering term in Eq. (19) is 6 dB below its maximum value. For example, the fall off should occur for frequencies above approximately 460 Hz for a correlation length scale of

0.5 meter. For frequencies below the resonant scattering threshold, we can expect the RL to rise proportional to the frequency dependence of the scattering kernel. Perturbation type scattering kernels have a magnitude which increases proportional to frequency squared. Thus for these types of kernels, the theory predicts that the RL grows proportional to frequency squared below the "resonance" frequency, and falls off faster than any power of frequency above it.

Although the theory cannot explicitly account for correlation function behavior consistent with power law distributions, it may be easily generalized that the high frequency asymptote for fractal [8] bottoms with dimension 2 ($k^{-3/2}$ dependence) will be proportional to $f^{1/2}$, and that for surfaces with a fractal dimension of 3 (space filling, very rough bottoms with $k^{-1/2}$ dependence) the RL will grow proportional to $f^{3/2}$ beyond the "resonance" frequency. In no case should these types of arguments be taken for frequencies above the range of validity of the perturbation approximation itself.

In Fig. 15 the frequency dependence of the RL for scattering from a water-sediment interface roughness with a correlation length scale of 0.5 m is shown for the 20 Hz bandwidth case. The maximum RL is seen to occur at 300 Hz. Our simple relation predicts a maximum RL at 230/0.5 or approximately 460 Hz. It may also be seen from the results that the RL increases roughly 6 dB between 150 and 300 Hz, as is predicted for perturbation theory. Between 75 and 150 Hz the increase is larger, probably because the bottom impedance contrast at 75 Hz is much lower and this causes a substantial additional decrease in the RL over the 6 dB which would be predicted for scattering from homogeneous boundaries alone.

3.3 Effect of bandwidth on RL

In the development of the theory it became evident that as bandwidth of the interrogating waveform is increased, the amount of coherent structure expected in the RL is decreased. This is shown through numerical example in Figs. 16 through 19 for the four frequencies of interest. The results are shown both for water-sediment and sediment-subbottom interface scattering. As before, the sediment-subbottom scattering results have much the same or less coherent propagation structure and lower overall levels. Since some of the lower order modes do not penetrate to the sediment-subbottom interface, some of the coherent propagation structure from the sediment-subbottom scattering interface for the very small bandwidths may be reduced.
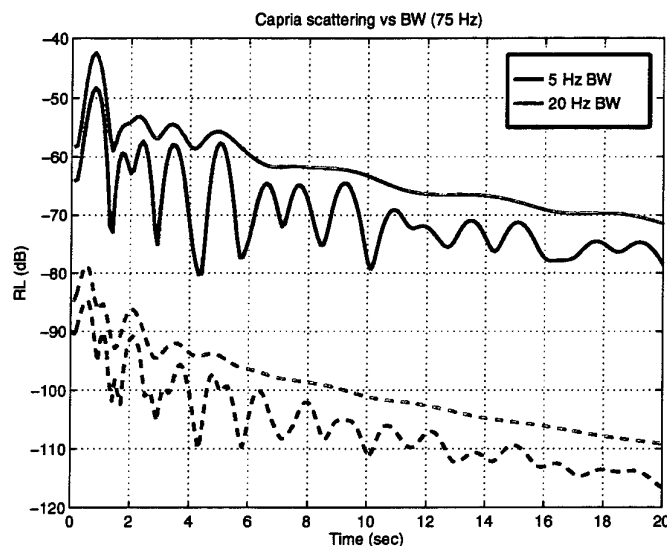

Figure 16 *The RL as a function of bandwidth at 75 Hz. The correlation length scale is 0.5 m. As the bandwidth increases, the structure caused by the coherent interference of the modes is substantially decreased. The solid curves represent the reverberation expected from a rough water-sediment interface; the dashed results are for reverberation from the sediment-subbottom interface.*

In Fig. 16 the RL expected from a surface with a 0.5 m correlation length scale is indicated for processing bandwidths of 5 and 20 Hz at a 75 Hz center frequency. The solid curves represent scattering from the water-sediment interface roughness of rms amplitude 1 m, and the dashed curves represent scattering from the same amplitude roughness at the sediment-subbottom interface. The RL caused by the sediment-subbottom scatterers is seen to be approximately 30 dB lower than the water-sediment interface result, which is consistent with the fact that the scattering kernel itself is about 20 − 40 dB lower. The results for the 20 Hz bandwidth are

significantly smoother than the 5 Hz bandwidth results, and it can also be seen that there are slight differences between the coherent structure of the RL for scattering from the two different interfaces.
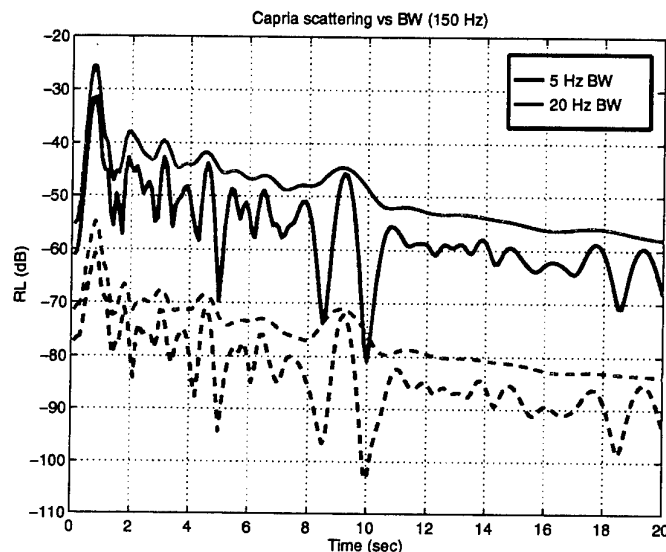

Figure 17 *RL as a function of bandwidth at 150 Hz. A strong forward propagation feature at 9 seconds is less discriminated as the bandwidth increases. This smearing of the strong bottom ensonification return in time for higher bandwidths is a conse- quence of the smaller number of modes interrogating this part of the bottom at any given time. The lack of a strong cancellation phenomena on either side of the conver- gence zone is also a function of the smaller individual patch size of the interrogating modes. As before, the solid curves show reverberation from a rough water-sediment interface; the dashed results are reverberation from the sediment-subbottom interface.*

The 150 Hz result in Fig. 17 shows that the strong return near $T = 9$ seconds for 5 Hz of bandwidth is also predicted to be seen for 20 Hz of bandwidth, but the strength of the return is spread out over more time due to the smaller number of modes interrogating the patch at any given time. In the sediment the scattering results are roughly the same, with approximately 30 dB less scattering strength. The same is true for the 300 Hz case illustrated in Fig. 18 and the strong return predicted at 16 seconds. For 20 Hz of bandwidth, the strength of this return is attenuated in relation to the returns from neighboring times, and for 80 Hz of bandwidth the structure all but disappears for times greater than about 4 seconds. For the 600 Hz case in Fig. 19, bandwidths up to 160 Hz are considered, and it is interesting to note that the RL features associated with ray like interactions with the bottom continue to be visible even at this bandwidth.
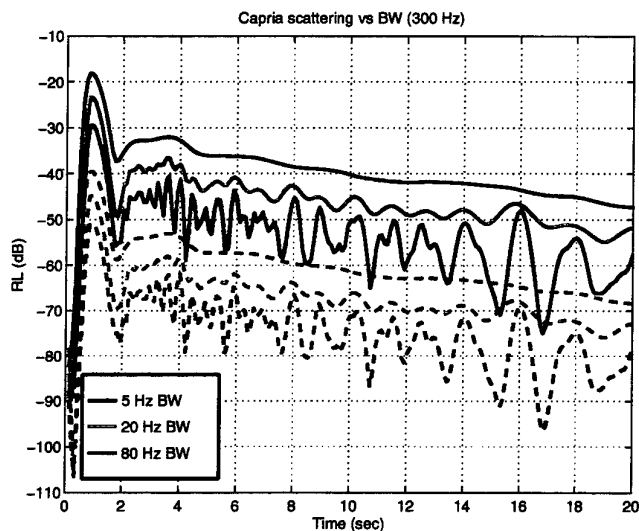
Figure 18 *RL as a function of bandwidth at* 300 *Hz. Strong bottom interactions at round trip travel times of* 8 *and* 16 *seconds are clearly seen in the* 5 *and* 20 *Hz bandwidth case, but at* 80 *Hz of bandwidth, the RL retains very little predictable structure.*
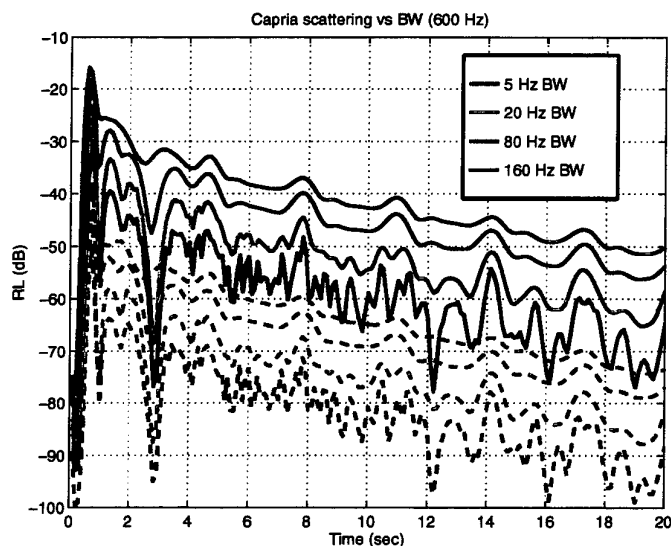

Figure 19 *The RL as a function of bandwidth at* 600 *Hz. Results for* 5, 20, 80 *and* 160 *Hz of bandwidth are illustrated in blue, green, magenta and red, respectively. Very strong bottom interactions at round trip travel times of* 5, 8, 11, 14 *and* 17 *seconds are visible at all the bandwidths, but with less resolution at the highest bandwidths.*

3.4 Effect of correlation length scale on RL

As discussed above, for any correlation length scale there exists a *resonance frequency* at which the RL is maximized. At fixed frequency and for narrow bandwidths, there is a related *resonance correlation length scale* with a magnitude of $\ell_r \simeq 230/f$. For scatterers with correlation length scales longer than the resonance correlation length scale, the RL is predicted to decrease proportional to $e^{-\ell^2/\ell_r^2}$.
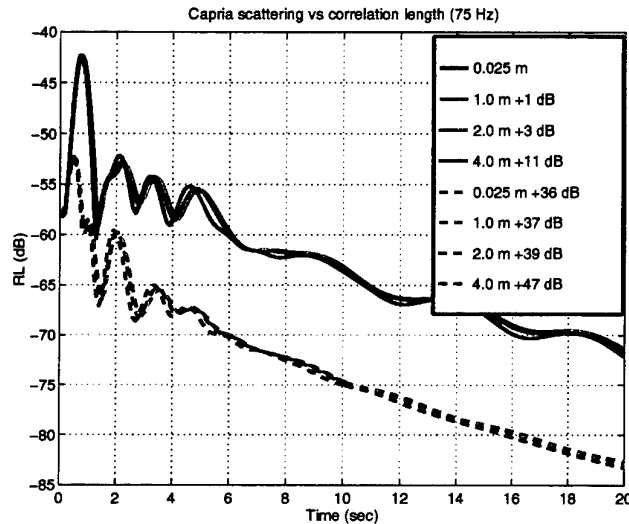

Figure 20 *The effect on the structure of the RL at 75 Hz caused by changes in the correlation length scale. In general, only the 4.0 meter correlation length scale is seen to cause an observable change in the RL, however it is not a signature which one would expect to be observable in data. Overall levels in the RL have been removed in this figure. The amount to be added to the various levels is indicated in the legend.*

In Figs. 20 through 23 the effect of correlation length scale is shown for water-sediment and sediment-subbottom rough surface scattering as a function of center frequency. All results are computed using a bandwidth of 20 Hz. Correlation length scales considered vary between 0.25 to 4 m. As indicated in Fig. 20, at 75 Hz only the 4 m correlation length scale is greater than ℓ_r. To ease comparison between the results, all the curves have been normalized up to the RL level for scattering from the 0.25 m correlation length scale roughness. The solid curves represent the RL for water-sediment interface scattering, and the dashed curves indicate the RL caused by sediment-subbottom interface scattering. The amount the curves have been moved is indicated in the legend. Inspection of the results shows that the RL for the 4 m roughness has slightly different structure in comparison to the RL caused by the shorter correlation length scales, and that the RL has roughly 11 dB less intensity for the 4.0 meter correlation length scale in comparison to the results
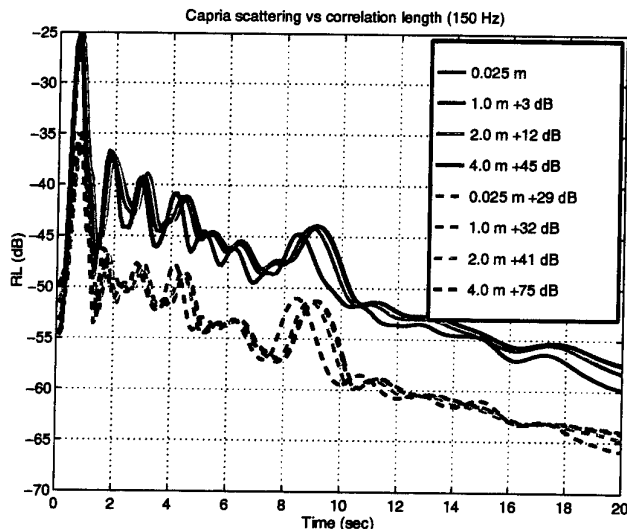
Figure 21 *RL as a function of correlation length scale at* 150 *Hz. Here both the* 4.0 *and the* 2.0 *meter correlation length scales have observably different structures from the shorter length scales. Of these, the* 4.0 *meter correlation length scale effect might be observable in data.*

for the shorter length scales. The results for the shorter correlation length scales are virtually identical both in structure and in intensity, with only 3 dB difference between them. The RL for sediment-subbottom interface scattering is approximately 46 dB lower, and shows remarkably less structure at late time, due to the fewer number of modes interacting strongly with the sediment-subbottom interface. As with the water-sediment interface results, the RL for the 4 m correlation length scale is approximately 10 dB lower than for the shorter correlation length scales.

At 150 Hz, Fig. 21 indicates that both the 2 and the 4 meter correlation length scale roughnesses cause substantially less RL than the shorter length scales. This is in agreement with the predicted resonance length ℓ_r of 1.5 m for this frequency. The properties of the Gaussian correlation function imply that scattering from correlation length scales much longer than the resonance length becomes vanishingly small at a rate faster than any power of ℓ^2/ℓ_r^2. This is a pathology which is the cost of using the easily integrable Gaussian correlation function in the derivation of the theory and is not expected to represent the behavior of scattering from real world roughness profiles. The result as it stands is that the RL from the water-sediment interface roughness with the 4 m correlation length scale is expected to be 45 dB lower than the RL from the same interface with a 1 m correlation length scale. Of more interest is the change in the structure of the RL for increasing correlation length scale, which is more pronounced than at 75 Hz. This change represents the
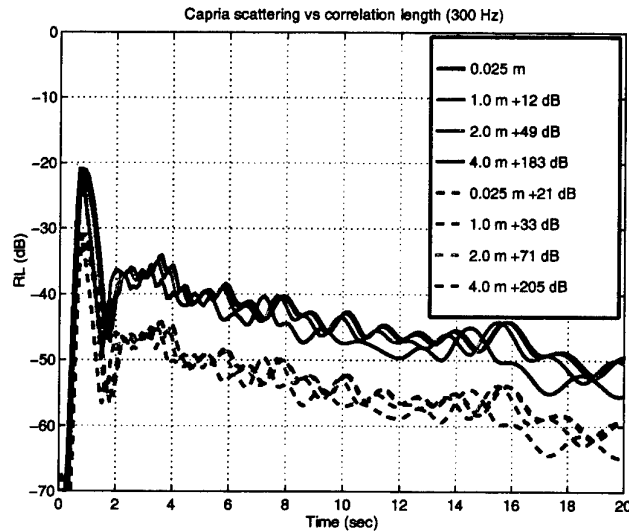
Capria scattering vs correlation length (300 Hz)

Figure 22 *RL as a function of correlation length scale at* 300 *Hz. As in the* 150 *Hz case, only the* 4.0 *meter correlation length scale causes a significant and measurable change in the expected structure of the reverberation.*

signature of correlation length scale predicted to be observable from experiments.

As at 75 Hz, the RL caused by sediment-subbottom scattering at 150 Hz is seen to be about 40 dB lower than for water-sediment scattering. The structure differences between these results, along with the lower overall levels, are the signatures which distinguish the two scattering mechanisms from one another. In this example the strong feature in the RL at 8.5 seconds is predicted to be more prominent for sediment-subbottom scattering than for water-sediment scattering, while the earlier features in RL are less prominent.

In Fig. 22 the effect on RL of the various correlation length scales at 300 Hz continues to become more pronounced, but the differences between the RL for water-sediment and sediment-subbottom scattering seems to become less evident. At this frequency, the resonance length scale is .75 m, and even the response from 1 m roughness is 12 dB lower than from 0.25 m roughness. The response from the 4 m roughness is now approximately 130 dB lower than the 2 m response, consistent with the rapid falloff of the Gaussian roughness power spectrum for correlation length scales much larger than ℓ_r. Again, this result is not representative of what one would expect for more realistic roughness profiles, but the structural differences in the RL which accompany the increase of the correlation length scale are expected to occur for all types of roughness profiles and therefore represent a signature of correlation length scale in the RL.
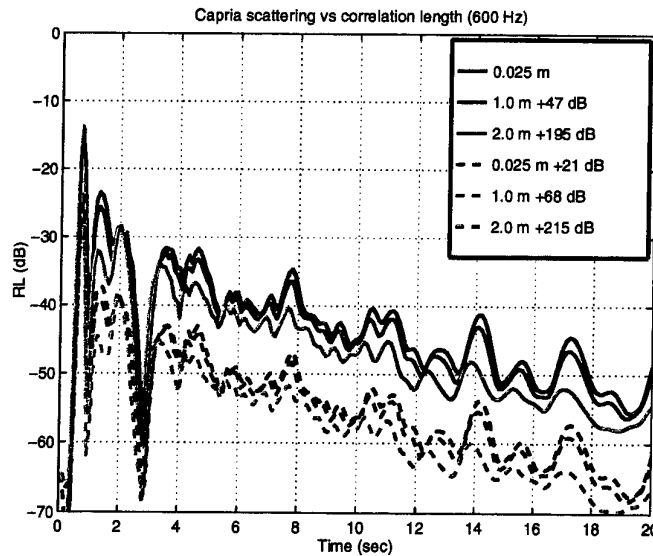
Capria scattering vs correlation length (600 Hz)

Figure 23 *RL as a function of correlation length scale at 600 Hz. Here an interesting change in the RL features associated with convergence zones on the bottom is noticed for the 2.0 meter correlation length scale. Due to the very rapid drop-off of the Bragg scattering term from the lightly attenuated lower order modes, the RL observed to come from these features is attenuated by 5-8 dB.*

The sensitivity of the RL to correlation length scale at 600 Hz is illustrated in Fig. 23. There is a very evident signature of decreasing response at the ray cycle times (8, 11, 14 and 17 seconds) with increasing correlation length scale, while again the difference between the RL caused by the water-sediment and the sediment-subbottom scattering mechanisms seems to lie mostly in the overall decrease in the scattering levels for the latter mechanism. The magnitude of these differences in the RL between two mechanisms will be dependent on the magnitude of the angular differences between the effective scattering kernels.

3.5 Comparison of closed form and Monte-Carlo solutions

To verify that the behavior of the closed form solution in Eq. (16) for the ensemble average of the short time average of the reverberation intensity is in agreement with what one would obtain by taking an actual ensemble of independent backscattered intensity observations, a modified version of Eq. (9) for the backscattered pressure was implemented where the azimuthal integral was implicitly performed by replacing the scatterer density in range and azimuth $\eta(r, \theta)$ with an effective scatterer density explicit in range only whose standard deviation falls off proportional to one over the square root of the scatterer range, consistent with the expression for the effective one dimensional scatterer variance derived in Annex A

$$\hat{\eta}(r) = \eta(r, \theta)|_{\theta = \theta_{ref}} \frac{(2\pi)^{1/4}\pi}{\sqrt{r\ell}}. \qquad (21)$$

In this case Eq. (8) may be rewritten as a range integral only involving the known narrowband properties of the waveguide as defined in Section 2

$$\begin{aligned}
p(t, z_s, z_r) &= A\Re \left\{ e^{-i\omega_o t} \sum_{m=1}^{N} \sum_{n=1}^{N} \sigma_{nm} \frac{\phi_m^o(z_s)\phi_m^{o-}\phi_n^{o+}\phi_n^o(z_r)}{\sqrt{k_n^o k_m^o}} \right. \\
&\quad \times \left. \int_0^{\infty} dr\, \hat{\eta}(r) e^{i(k_n^o + k_m^o)r} e^{-(t - S_{nm}r)^2/4\sigma_{nm}^2} \right\}. \qquad (22)
\end{aligned}$$

The transformation in Eq. (21) has the property that the ensemble average of the square of Eq. (22) is identically equal to Eq. (16) for Gaussian distributed correlation functions. Comparisons between the ensemble average of the square of Eq. (22) averaged over 50 realizations of the effective one dimensional scatterer realizations in Eq. (21) are illustrated in Figs. 24 through 27 for a source depth of 10 m, a receiver depth of 20 m, and a correlation length scale of 0.5 m. For the 75 and 150 Hz center frequency examples, results are shown for bandwidths of 5 and 20 Hz. For the 300 Hz example in Fig. 26, results are shown for 5, 20 and 80 Hz of bandwidth, and for the 600 Hz example in Fig. 27, results are shown for 5, 20, 80 and 160 Hz of bandwidth. All the results in general show very good agreement between the Monte-Carlo ensemble averages and the closed form expressions, and serve as an important verification of the closed form expressions.

It is important to make some observations on the relative merits of evaluating the closed form expressions for estimating the ensemble average through the Monte-Carlo technique discussed here. First, at very low frequency, the closed form expressions are almost always faster to evaluate than the Monte-Carlo results. The reason is that as frequency decreases, the requirements on the spatial sampling of the range integral in Eq. (22) become dictated by the correlation length scale of the scatterer distributions, and therefore the computational effort remains constant
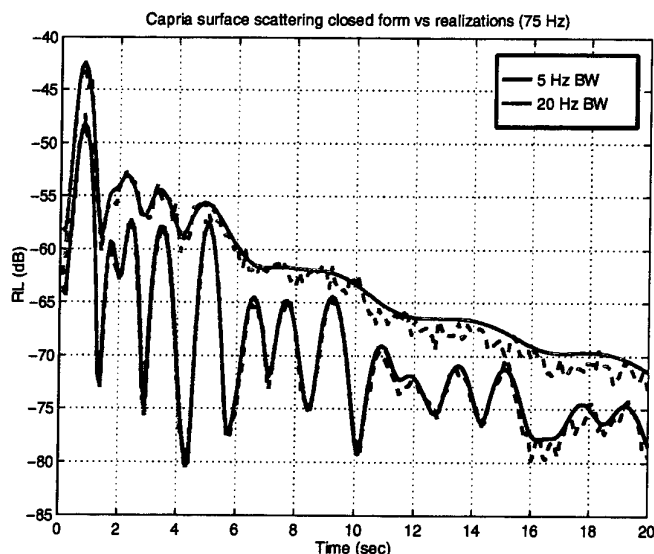
Capria surface scattering closed form vs realizations (75 Hz)

Figure 24 *Comparison between closed form solution for RL (solid) and the Monte-Carlo result (dashed) for 5 and 20 Hz of bandwidth at 75 Hz. The agreement is good, particularly for the 5 Hz bandwidth case. Agreement for the 20 Hz bandwidth case could likely be improved through a broadening of the evaluated portion of the range integral at late time in the Monte-Carlo calculation, as discussed in the text.*

with frequency below frequencies where the wavelengths become long with respect to correlation length scale. On the other hand, as frequency increases, the spatial sampling in Eq. (22) becomes dictated by the wavelength of the acoustic waves as they become shorter than the correlation length scale (in practice, the roughness was sampled at the lesser of every $\ell/10$ or every $\lambda/8$.) But at frequencies where a large number of modes become propagating, the evaluation of the four dimensional modal summation in the closed form expression in Eq. (16) rapidly becomes impossible.

Several steps have been taken in the software which evaluates Eqs. (16) and (22). In order to speed up the four dimensional modal summation in Eq. (16), the leading term in the modal coherence term Eq. (18) are evaluated, and the calculation inside the four dimensional modal summation loop only proceeds if the argument to the exponent is greater than that the argument for the highest order mode minus ten, so that only modal cross terms of -43 dB and higher relative to the highest order mode (neglecting the attenuation due to the imaginary part of the wavenumbers) are included. This step significantly decreases the computation at late times when the returns from the various modes become uncorrelated, offering factors of 4-10 in performance gain. Of course this threshold is adjustable and could be further tuned.

For the efficient evaluation of the range integrals in Eq. (22), the integrals are truncated to evaluate contributions only from scatterers which are in the immediate
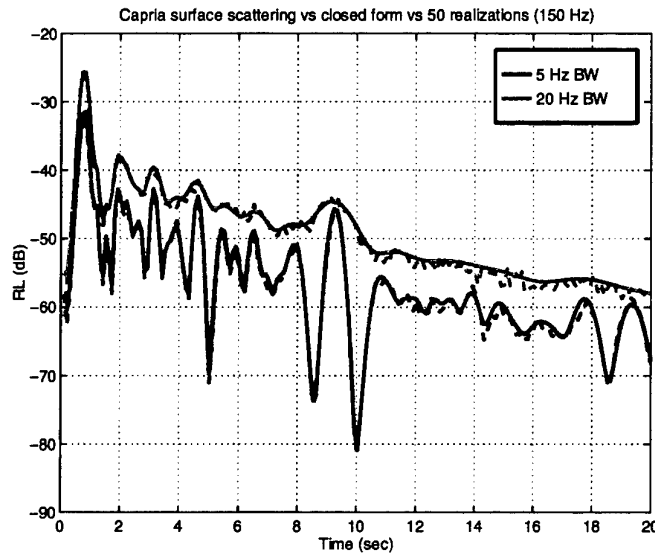
$- 36 -$

Figure 25 *Comparison between the closed form (solid) and Monte-Carlo (dashed) RL at 150 Hz. The excellent agreement for 5 and 20 Hz of bandwidth gives confidence that the closed form expressions are correct.*

vicinity of the stationary range $r_S = t/S_{nm}$ at the desired time t. The truncation is determined by seeking the solution for the range increment Δr on either side of the r_S where the envelope function $\exp\{-(t - S_{nm}(r \pm \Delta r))^2/\sigma_{nm}^2\}$ was equal to -60 dB. For very broad bandwidths, the denominator $\sigma_{nm}^2 \equiv 4/\Delta\omega^2 - i2D_{nm}r$ becomes quite complex, and the solution is no longer obtainable by the quadratic rule, as the envelope function become highly oscillatory in range, with an extended envelope as discussed at the beginning of this section. In these cases, especially the 80 Hz bandwidth case for 300 Hz and both the 80 and the 160 Hz bandwidth cases for 600 Hz, the range integrals had to be significantly extended around the stationary range to get good agreement between the closed form solutions and the ensemble average. The computational cost of these extensions of the range integral was very high. In cases like these evaluation of the closed form expressions has clear computational advantages.

In general, one may summarize the tradeoff between the closed form expressions and the Monte-Carlo technique by stating that the closed form expressions have the value that 1) they provide insight, and that 2) they are more efficient to calculate at low frequencies. The Monte-Carlo solutions provide no insight *per se*, but at higher frequencies for moderate bandwidths they are more efficient to calculate. However, as we discuss in the next subsection, the Monte Carlo solutions offer the additional outstanding opportunity to evaluate backscatter from scatterer distributions which are spatially correlated in a non-Gaussian way. The Gaussian assumption places a
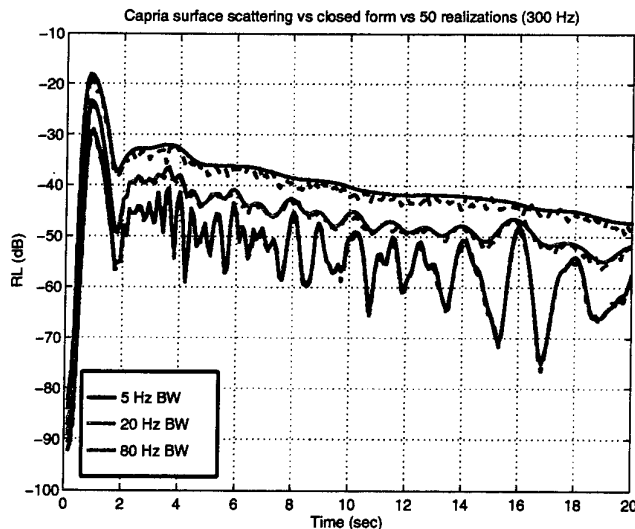
Capria surface scattering vs closed form vs 50 realizations (300 Hz)

Figure 26 *Comparison between the closed form (solid) and Monte-Carlo (dashed) expressions for the RL at 300 Hz for 5, 20 and 80 Hz of bandwidth. To get reasonable agreement between the two results at 80 Hz of bandwidth, the spatial extent of the range integral over the scatterer distributions needed to be significantly extended in the Monte-Carlo result, as discussed in the text.*

very unrealistic restriction of the closed form theory. The ability to treat general scatterer correlation functions is perhaps the most outstanding capability offered by the Monte-Carlo solution technique.
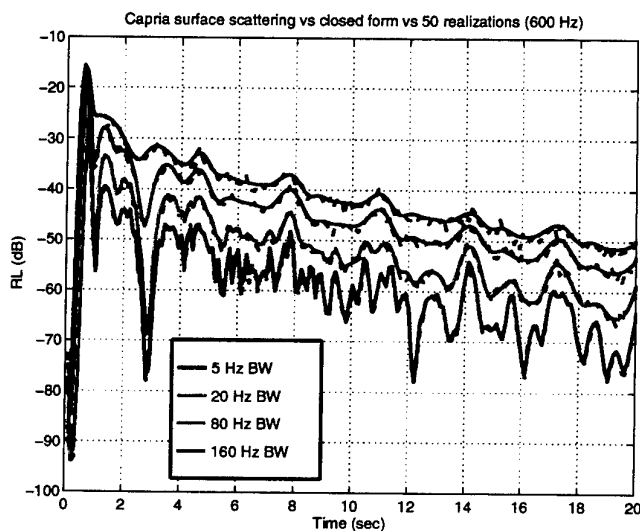
Figure 27 *Comparison between closed form (solid) and Monte-Carlo (dashed) expressions for the RL at 600 Hz for 5, 20, 80 and 160 Hz of bandwidth, indicated by the blue, green, magenta and red curves, respectively. The agreement in all cases is very good, giving confidence that the closed form expressions are correct. As mentioned in the text, the range integrals were significantly extended about the stationary range in order to have the Monte-Carlo results for 80 and 160 Hz of bandwidth agree with the closed form expressions.*

3.6 Effect of correlation function form on RL

Aside from providing the opportunity to perform an internal consistency check on the closed form expression for the ensemble average of the short time average of reverberation intensity, Eq. (22) also has the additional value that scattering from roughness profiles with various non-Gaussian correlation properties may be evaluated and compared to one another and the Gaussian results. Almost all real world scatterer distributions have non-Gaussian spatial correlation characteristics. The most typical spatial correlation properties, which involve surfaces of various fractal dimensions, yield power spectra which are distinctly non-Gaussian and instead obey an inverse power law in the spatial wavenumber [8]. The effect of these more realistic scatterer distributions is that as the resonant wavenumber $k_n + k_m$ increases for Bragg scattering, the backscatter falls off much more slowly ($\propto (k_{nm}\ell)^{-(2-4)}$) than in the case of Gaussian scatterer spectra ($\propto \exp\{-(k_{nm}\ell)^2\}$.) Not only does this imply that the mean levels of the reverberation are higher for surfaces which are correlated in a fractal way, but also that the components backscattered from lower order modes (which give larger resonant wavenumbers) can give a much larger contribution to the total backscatter from fractal scatterers than from Gaussian correlated scatterers, in those cases where the correlation length scale is longer than a wavelength.
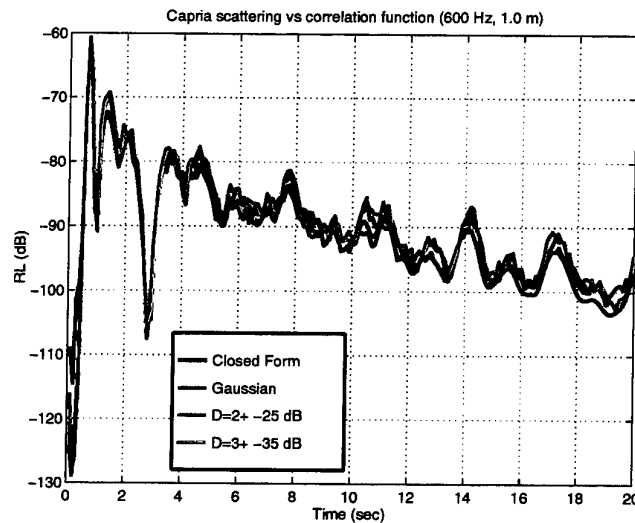
Figure 28 *RL at 600 Hz for various scatterer distributions with a correlation length scale of 1.0 m. The power law scatterer spectra cause significantly more backscatter from the regions of strong constructive bottom interaction*

The difference between the backscattered intensity from scatterers with Gaussian and non-Gaussian correlation properties at 600 Hz is illustrated in Figs. 28 and 29.
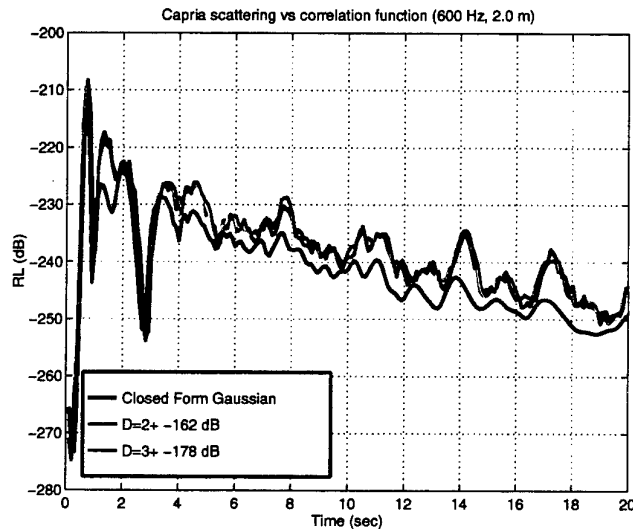
Capria scattering vs correlation function (600 Hz, 2.0 m)

Legend:
- Closed Form Gaussian
- D=2+ −162 dB
- D=3+ −178 dB

Figure 29 *RL at* $600Hz$ *for Gaussian, and two power law scatterer distribution power spectra with a correlation length scale of* 2.0 *m. The very low Bragg scattering component into the lower order modes in the Gaussian case significantly reduces the backscattering contributions associated with the strong bottom interactions at* 8, 11, 14 *and* 17 *seconds.*

The results in Fig. 28 show that for a correlation length scale of 1.0 m, the backscatter from convergence zone type propagation features on the bottom is much more pronounced for 2-D surfaces with fractal dimension 2 to 3 (magenta and green curves, respectively) than it is for the Gaussian surfaces (shown in black for closed form and in red for Monte-Carlo,) by a factor of about 2-3 dB. Since the lower order modes suffer less propagation loss at long range, and they scatter more from the fractal surfaces, the increase becomes more pronounced at later times. This effect can be seen even more dramatically in Fig. 29, where for a correlation length of 2.0 m the propagation induced structure to the reverberation intensity is much more pronounced for the two fractal surfaces than it is for the Gaussian surface.

3.7 Spatial-temporal coherence of monostatic backscatter

The closed form theory or the Monte-Carlo results may be used to estimate the coherence of the backscatter as a function of vertical separation and time after shot [2]. The coherence between the receiver pair $[z_1, z_2]$ on a vertical line array at time t is given in Eq. (12) as

$$\rho^2(t, z_1, z_2) = \frac{p_{STA}^2(t, z_1, z_2)}{\sqrt{p_{STA}^2(t, z_1, z_1)p_{STA}^2(t, z_2, z_2)}}.$$

This quantity was evaluated for the four frequencies of interest at 5, 10, 15 and 20 seconds and plotted as a function of z_1 and z_2 for 5 Hz of bandwidth in Figs. 30 through 33. The results indicate a decrease in spatial coherence for very large offsets at late time. The decrease in coherence for large receiver separation is caused by the modal decorrelation discussed throughout this report. Since the spatial coherence may be thought of as a *change of basis* on the modal coherence, a decrease in inter-modal coherence implies directly the reduced spatial coherence observed in these results.

In Figs. 34 through 37, the vertical coherence at 75, 150, 300 and 600 Hz are il-lustrated for 20 Hz of bandwidth. The decrease in spatial coherence at late time becomes stronger as bandwidth is increased. For example, the results in Fig. 34 show that the coherence between receivers at different depths at 600 Hz for 20 Hz of bandwidth is already as decorrelated at 5 seconds as Fig. 33 indicates they are at the same frequency with only 5 Hz of processing bandwidth a full 20 seconds after the shot.

These vertical coherence results are anticipated to be useful as they serve to provide a very important quantity for evaluating the performance of various signal processing algorithms for active detection in reverberation limited environments. These results also can be used as constraints in the design of processors which are more robust to waveguide reverberation.

---

[2]In the present formulation of the closed form solution, the coherence between two receivers at two different times cannot be obtained, although the modification of the theory to yield this result presents no foreseeable difficulties.
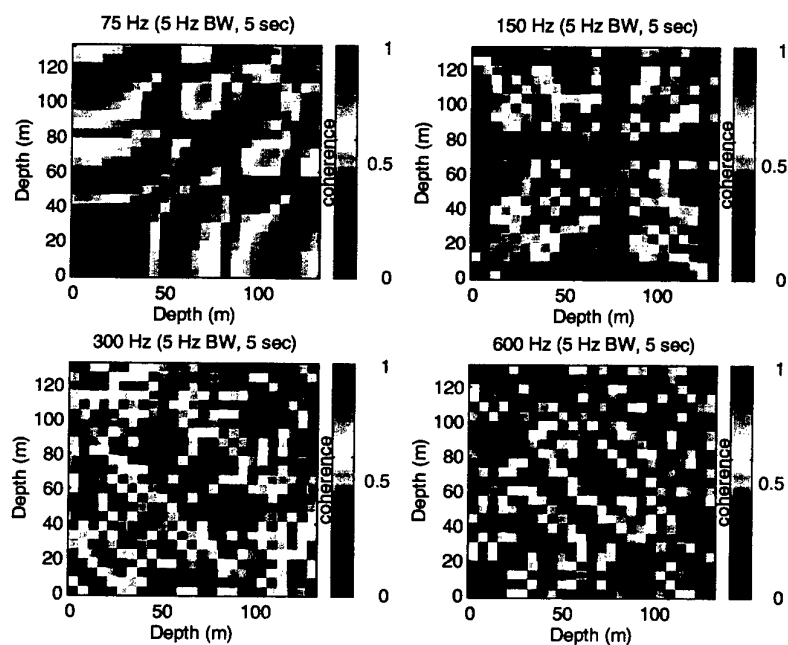
Figure 30 *Vertical coherence 5 seconds after the shot for 5 Hz of processor bandwidth. The results show strong vertical coherence even at large receiver offset, especially at 75 Hz.*
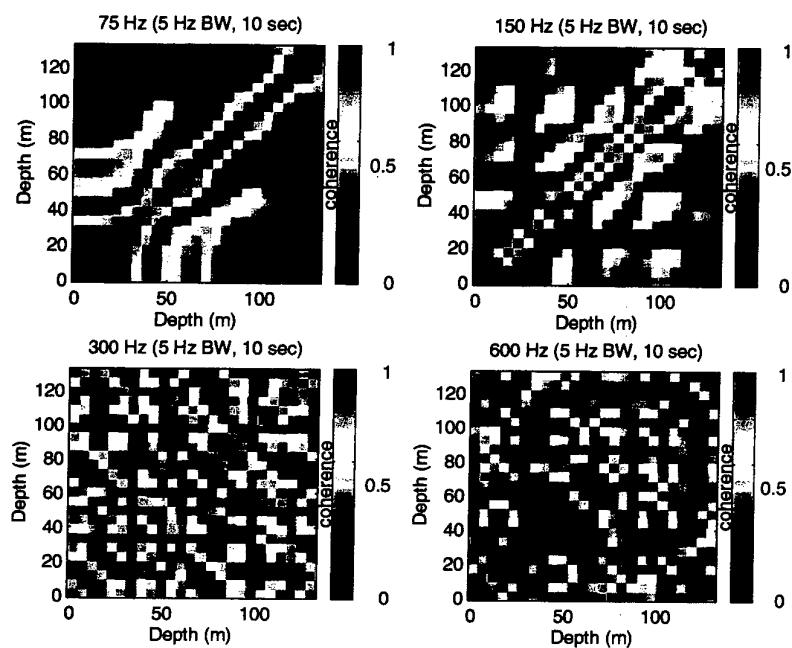
Figure 31 *Vertical coherence for 5 Hz of processing bandwidth 10 seconds after the shot. The results at 75 and 150 Hz are more banded than at 5 seconds. The results at 300 and 600 Hz shows high off-diagonal correlation and some underlying structure which appears undersampled.*
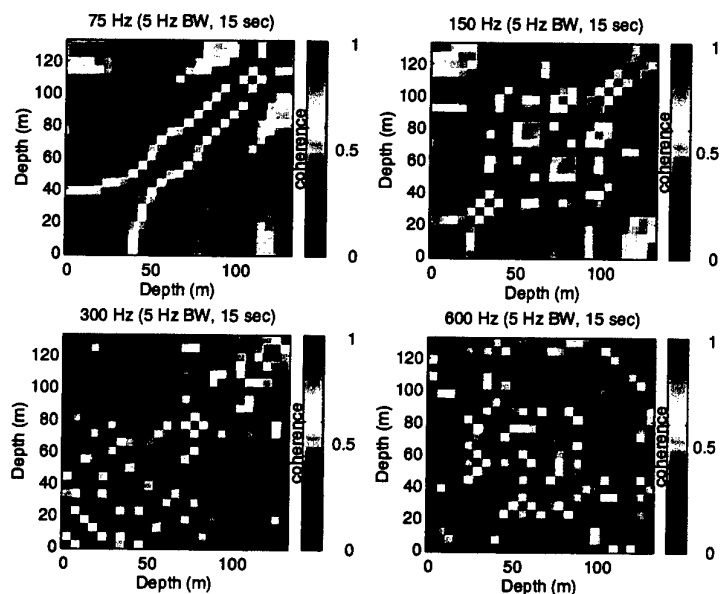
Figure 32 *The vertical coherence 15 seconds after the shot for 5 Hz of processing bandwidth. The results at 75 and 150 Hz have become more diagonalized, but all the results continue to show quite high coherence for large receiver offsets. A trend towards increasing spatial coherence near the source depth of 10 m is noticeable.*
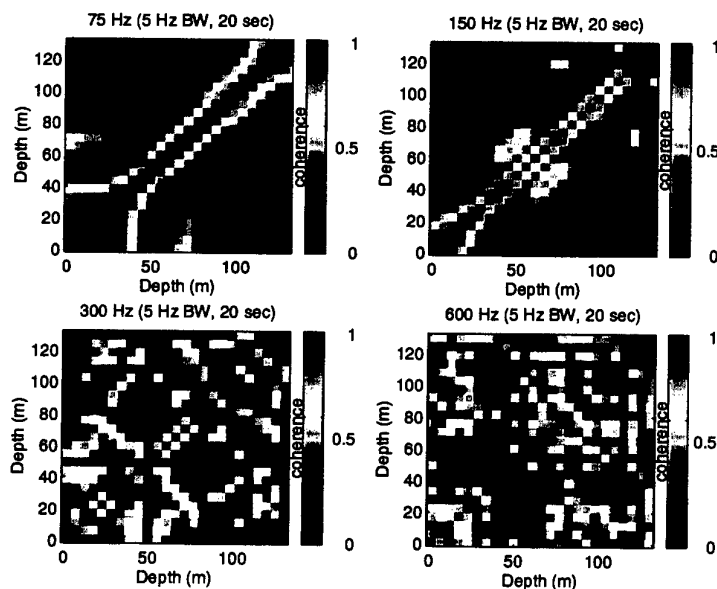

Figure 33 *Vertical coherence at 600 Hz for 5 Hz of processing bandwidth 20 seconds after the shot. Results at 300 and 600 Hz continue to show larger off-diagonal coherence.*
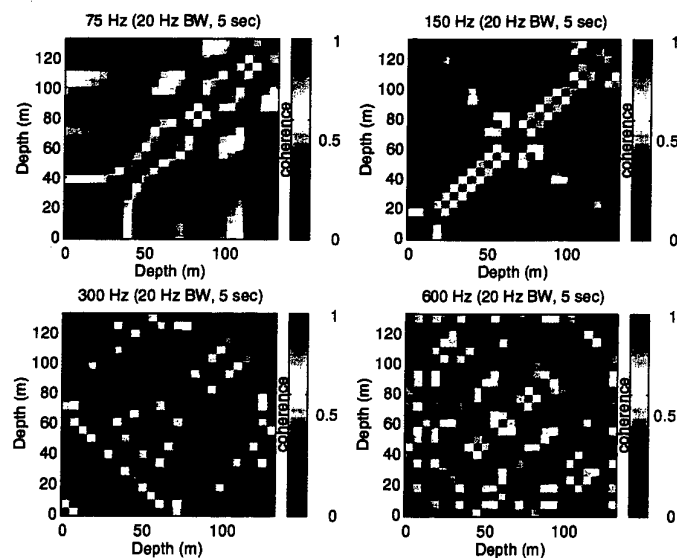
Figure 34 *Vertical coherence at 5 seconds after the shot for 20 Hz of processing bandwidth. These results are much more diagonal than the results at the same time shown in* **Fig. 30** *for 5 Hz of bandwidth, and bear more of a resemblance to the 5 Hz results for 20 seconds after the shot illustrated in* **Fig. 33**.
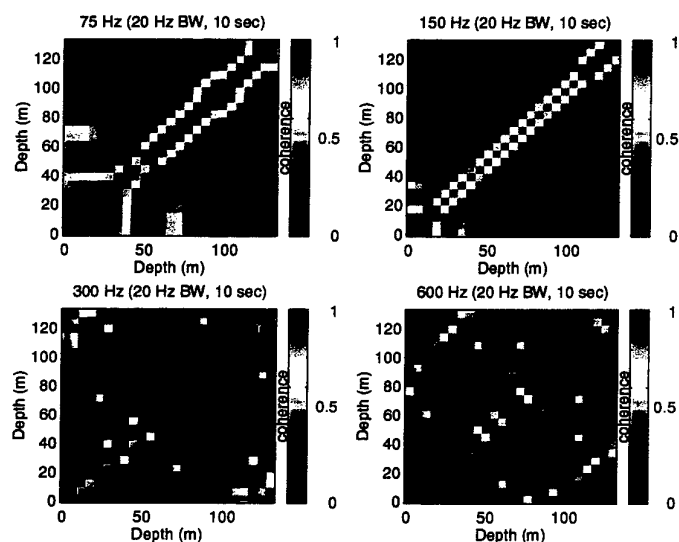

Figure 35 *The vertical coherence 10 seconds after the shot for 20 Hz of bandwidth. The results at 75 and 150 Hz are diagonalized. At the higher frequencies some off-diagonal structure is still observed. As in the coherence examples for 5 Hz of bandwidth, there is a trend towards increasing spatial coherence near the source depth of 10 m, especially at 75 and 150 Hz.*
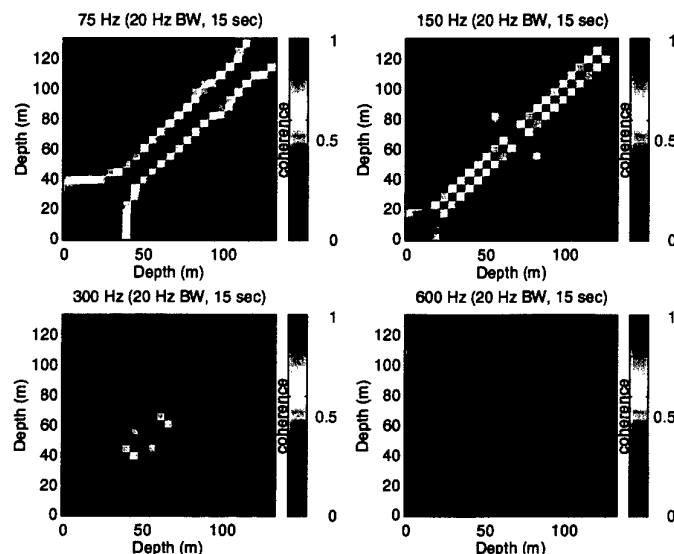
Figure 36 *The vertical coherence at 15 seconds for 20 Hz of bandwidth. Only the 600 Hz result retains significant off-diagonal structure. Note the decreasing width of the diagonal coherence structure with increasing frequency. The trend towards increasing spatial coherence near the source depth is continued.*

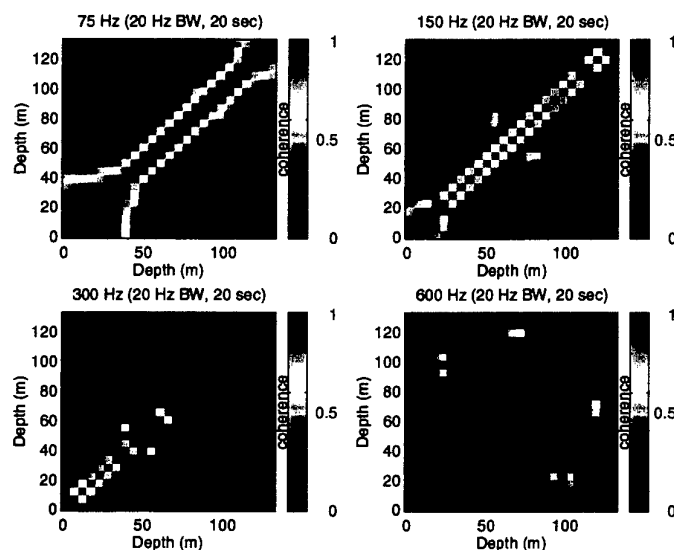**Figure 37** *Coherence at 20 seconds and 20 Hz of bandwidth. The results below 600 Hz are quite diagonal, with decreasing spatial coherence scale as frequency increases, as shown by the narrowing of the highly correlated region in the immediate vicinity of the main diagonal. The remaining off-diagonal coherence at 300 and 600 Hz is expected to go to zero as the bandwidth is further increased.*

4

Conclusion

The short time average of the monostatic backscattered reverberation intensity in a waveguide has been obtained as a function of 1) scatterer parameters of *i*) correlation length scale, *ii*) correlation function and *iii*) scatterer interface or depth, 2) the processing bandwidth parameter, and 3) the channel parameters of *i*) number of propagating modes, and *ii*) their associated wavenumbers, shapes, slownesses and curvatures, and *iii*) their ability to excite the scatterers. The results indicate that as processing bandwidth is increased, the predictable structure to the reverberation is decreased, with an accompanying decrease in the vertical coherence, at late time. The results also show that scatterer depth, for instance on the water-sediment interface, or at the sediment-subbottom interface, can significantly affect the levels, and the temporal characteristics of the received reverberation. Changes in the correlation length scale can also produce observable changes in the reverberation structure for otherwise fixed processing and channel parameters. For Gaussian correlated scatterers, a frequency of maximum reverberation is predicted, below which reverberation intensity grows proportional to frequency squared for perturbation theory scattering kernels, and above which the reverberation intensity falls off faster than any power of frequency.

Results obtained in this report also indicate that the spatial structure of the forward propagation has a very significant influence on the expected temporal structure of the reverberation. Convergence zones onto the scattering layer and other pathological features in the forward propagation can cause associated large peaks in the reverberation intensity at the appropriate round trip travel time. The characteristics of the reverberation features turn out to be well defined functions of the waveguide and scatterer parameters, the center frequency, and the bandwidth. Until now, most scattering theories have ignored the coherent interaction between the various propagation paths. The work presented here shows that these terms need not be neglected, that they can be treated in a robust way, and that when these terms are retained additional insights are gained into the rich physics of waveguide reverberation. In addition, since propagation induced features are commonly observed in reverberation data sets, retention of these terms is also an advantage for developing a better understanding of the features which are found in these data.

The closed form solutions of the short time average of the backscattered intensity developed in this report have been benchmarked against self-consistent Monte-Carlo

predictions, with good results. The Monte-Carlo predictions have also been used to predict the differences between the reverberation caused by Gaussian and non-Gaussian correlated scatterers. These results show the observability of scatterer correlation properties in the reverberation signature. The reverberation time series generator used to obtain the Monte-Carlo results also delivers a capability to evaluate the higher moments of the reverberation statistics for various scatterer correlation length scales, spatial correlation properties and amplitude distributions. Although this capability was not explored in this work, it is believed that this capability will prove valuable for developing an understanding of the non-Rayleigh distributions of reverberation intensity which are often observed in shallow water reverberation data [9].

In general, the theory enhances understanding of how waves interact with roughness to cause reverberation in waveguides. How the coherence between the backscattered modes is affected by time after shot, correlation length scale and patch size have all been rigorously identified in the closed form solution, and various limiting behaviors have been identified and discussed. In particular, the results show that for very narrow bandwidths, the traditional view of reverberation as Bragg scattering from patches of limited spatial extent is correct, but for very large bandwidths, Bragg scattering does not occur and reverberation levels are much higher and more spatially uncorrelated. The theoretical results also show that coherent interference structure between modes which interrogate different parts of the bottom can be expected when the correlation length scale is longer that the modal separation distance. These results, while heuristically predictable, are here explicitly given for the first time in terms of the various parameters which define a monostatic reverberation experiment.

Finally, the time-dependent coherence between the modes derived in this report has provided a means for predicting the vertical coherence in the waveguide as a function of relevant parameters. It is believed that this capability of the theory will prove useful for guiding the design of robust algorithms for active localization of targets in reverberation limited environments.

5

Acknowledgments

References

[1] D. D. Ellis, "A shallow water normal-mode reverberation model," J. Acoust. Soc. Am. 97, pp. 2804–2814, 1995.

[2] D. J. Tang, "Shallow water reverberation due to sediment volume inhomogeneities," Submitted to IEEE J. of Ocean Eng., Feb 8, 1996.

[3] C. Holland, "Capraia SCARAB," SACLANT Undersea Research Centre Cruise Report, La Spezia, Italy, July, 1997.

[4] D. F. Gingras and P. Gerstoft, "Inversion for geometric and geoacoustic parameters in shallow water: Experimental results," J. Acoust. Soc. Am. 97, pp. 3589–3598, 1995.

[5] C. Holland and J. Osler, "High resolution geoacoustic inversion in shallow water using a towed broadband source and a bottom moored receiver," manuscript in preparation, Sept. 1998.

[6] F. B. Jensen, "Comparison of transmission loss data for different shallow water areas with theoretical results provided by a three fluid normal-mode propagation model," in *Sound Propagation in Shallow Water*, edited by O. F. Hastrup and O. V. Olesen, CP-14, SACLANT Undersea Research Centre, La Spezia, Italy, pp. 79-92, 1974.

[7] M. B. Porter, "The KRAKEN Normal Mode Program", SACLANT Undersea Research Centre SM-245, La Spezia, Italy, 1991.

[8] J. A. Goff and T. H. Jordan, "Stochastic modeling of seafloor morphology: inversion of sea beam data for second order statistics", J. Geophys. Res. 93, 13589-13608, 1988.

[9] D. A. Abraham, "Modeling non-Rayleigh reverberation," SACLANT Undersea Research Centre SR-266, La Spezia, Italy, 1997.

Annex A

Evaluation of azimuth integrals

An anisotropic Gaussian correlation function with its major and minor axes aligned with the $x - y$ coordinate system has the following form

$$R_\eta = \frac{\langle \eta^2 \rangle}{2\pi \ell_x \ell_y} \exp(-x^2/2\ell_x^2 - y^2/2\ell_y^2)$$

which upon insertion of the change of coordinates given in Eqs. (14) is

$$\begin{aligned}
R_\eta &= \frac{\langle \eta^2 \rangle}{2\pi \ell_x \ell_y} \exp(-\theta''^2 \underbrace{(r^2 \sin^2\theta/2\ell_x^2 + r^2\cos\theta/2\ell_y^2)}_{A}) \\
&\times \exp(-\theta'' \underbrace{(2rr''\cos\theta\sin\theta(1/\ell_y^2 - 1/\ell_x^2))}_{B}) \\
&\times \exp(-\underbrace{(r''^2(\cos^2\theta/2\ell_x^2 + \sin^2\theta/2\ell_y^2))}_{C})
\end{aligned} \tag{23}$$

The change of coordinates in Eqs. (14) is explicit in the difference range r'' and angle θ'' between two scattering centers. If we assume that the scatterers are distributed homogeneously in space, then we may integrate over the difference angle θ'' without regard to the absolute angle θ. The solution is

$$\int_0^{2\pi} d\theta'' R_\eta = C_1 e^{-C} e^{B^2/4A} \int d\theta'' e^{-A\theta''^2} e^{-B\theta''} e^{-B^2/4A} \tag{24}$$

where $C_1 = \frac{\langle \eta^2 \rangle}{2\pi \ell_x \ell_y}$. The argument to the exponent in Eq. (24) is a perfect square. In the limit of range large in comparison to correlation length scale (almost always the case for times of practical interest,) the limits of the θ'' integral may be extended to plus and minus infinity. In this case Eq. (24) reduces to

$$\begin{aligned}
\int_0^{2\pi} d\theta'' R_\eta &= C_1 e^{-C} e^{B^2/4A} \sqrt{\pi/A} \\
&= \frac{\langle \eta^2 \rangle}{2\pi \ell_x \ell_y} \sqrt{\pi/(r^2\sin^2\theta/2\ell_x^2 + r^2\cos\theta/2\ell_y^2)} \\
&\times \exp(-(r''^2(\cos^2\theta/2\ell_x^2 + \sin^2\theta/2\ell_y^2))) \\
&\times \exp(\frac{r''^2(1/\ell_y^2 - 1/\ell_x^2)^2}{\sec^2\theta/2\ell_x^2 + \csc^2\theta/2\ell_y^2})
\end{aligned} \tag{25}$$

which upon some rearrangement gives Eq. (15).

Annex B

Evaluation of range integrals

To evaluate the r and r'' integrals in Eq. (16) we must first appeal to two approximations. The first approximation is that the range integrals over r and r'' both may be artificially extended to minus infinity. This approximation is found to be good for times greater than the pulse duration $2\pi/\triangle\omega$. For these times, all the scattering contributions come from ranges greater than zero, and so the scattering integrals may be artificially extended to minus infinity for the convenience of their evaluation.

The second approximation is that for the closed form evaluation of the scattering integrals, the explicit dependence of σ^2_{nm} and $\sigma^2_{n'm'}$ on range must be approximated by a dependence on time over round trip slowness S_{nm} (or $S_{n'm'}$)

$$\sigma_{nm} \simeq \triangle\omega^2(1 + iD_{nm}\triangle\omega^2 t/4S_{nm})^{-1}.$$

The same approximation is also required for the r^{-1} term in the denominator of the correlation function which was found in Annex A to result from the azimuthal integration of the scattering correlation function. This term is replaced by the approximation

$$r^{-1} \simeq S_{nm}/t.$$

This approximation is good when the range differential over the entire patch is a small fraction of the average range, a condition satisfied for

$$2\pi\omega_o/\triangle\omega k_{nm} \ll t\omega_o/k_{nm},$$

or for times much greater than one over the bandwidth of the pulse function in Hertz.

Use of the two above approximations allows the closed form evaluation of the range integrals through the use of standard techniques.

The first integral over r'' is evaluated in the following way. We square out any terms containing r'', and collect terms of various orders. Doing this, we find that we have the following terms quadratic, linear and independent of r'' in the exponent

$$
\exp\left(-\frac{\overbrace{\left(r^2\left(\frac{S^2_{nm}}{4\sigma^2_{nm}}+\frac{S^2_{n'm'}}{4\sigma^2_{n'm'}}\right)-r\left(\frac{S_{nm}t}{2\sigma^2_{nm}}+\frac{S_{n'm'}t}{2\sigma^2_{n'm'}}+i(K_{nm}-K_{n'm'})\right)+\frac{t^2}{4\sigma^2_{nm}}+\frac{t^2}{4\sigma^2_{n'm'}}\right)}^{C''}}{}\right)
$$

$$
\times\quad\exp\left(-r''\underbrace{(rS^2_{n'm'}/2\sigma^2_{n'm'}-tS_{n'm'}/2\sigma^2_{n'm'}+i(K_{n'm'}))}_{B''}\right)
$$

$$
\times\quad\exp\left(-r''^2\underbrace{(S^2_{n'm'}/4\sigma^2_{n'm'}+1/2\ell^2)}_{A''}\right),
\tag{26}
$$

where $K_{nm}=k_n+k_m$ and $K_{n'm'}=k_{n'}+k_{m'}$.

To complete the square we require a term of the form $-B''^2/4A''$ in the exponent. Adding this term inside the integral (and subtracting it away outside,) we can conveniently evaluate the r'' range integral for a contribution of

$$
\sqrt{\pi/A''}e^{B''^2/4A''}e^{-C''}=\sqrt{\pi/(S^2_{n'm'}/4\sigma^2_{n'm'}+1/2\ell^2)}
$$

$$
\times\quad\exp\left(\frac{S^2_{n'm'}(S^2_{n'm'}r^2-2S_{n'm'}rt+t^2)/4\sigma^4_{n'm'}+iS_{n'm'}K_{n'm'}(S_{n'm'}r-t)/\sigma^2_{n'm'}}{(S^2_{n'm'}/\sigma^2_{n'm'}+2/\ell^2)}\right.
$$

$$
\left.-\frac{K^2_{n'm'}}{(S^2_{n'm'}/\sigma^2_{n'm'}+2/\ell^2)}\right)
$$

$$
\times\quad\exp\left(-\left(r^2\left(\frac{S^2_{nm}}{4\sigma^2_{nm}}+\frac{S^2_{n'm'}}{4\sigma^2_{n'm'}}\right)-r\left(\frac{S_{nm}t}{2\sigma^2_{nm}}+\frac{S_{n'm'}t}{2\sigma^2_{n'm'}}+i(K_{nm}-K_{n'm'})\right)\right.\right.
$$

$$
\left.\left.+\frac{t^2}{4\sigma^2_{nm}}+\frac{t^2}{4\sigma^2_{n'm'}}\right)\right).
\tag{27}
$$

Eq. (27) remains under the r range integral, and contributes to its kernel, which may be rearranged into exponential powers Ar^2, Br and C which are quadratic, linear and independent in r respectively

$$\exp\left(-r^2\underbrace{\left(\frac{-S_{n'm'}^4/4\sigma_{n'm'}^4}{S_{n'm'}^2/\sigma_{n'm'}^2+2/\ell^2}+\frac{S_{nm}^2}{4\sigma_{nm}^2}+\frac{S_{n'm'}^2}{4\sigma_{n'm'}^2}\right)}_{A}\right)$$

(28)

$$\times\quad\exp\left(-r\underbrace{\begin{pmatrix}\frac{S_{n'm'}^3t/2\sigma_{n'm'}^4-iS_{n'm'}^2K_{n'm'}/\sigma_{n'm'}^2}{S_{n'm'}^2/\sigma_{n'm'}^2+2/\ell^2}-\frac{S_{nm}t}{2\sigma_{nm}^2}-\frac{S_{n'm'}t}{2\sigma_{n'm'}^2}\\-i(K_{nm}-K_{n'm'})\end{pmatrix}}_{B}\right).$$

$$\times\quad\exp\left(-\underbrace{\left(\frac{t^2}{4\sigma_{nm}^2}+\frac{t^2}{4\sigma_{n'm'}^2}-\frac{t^2S_{n'm'}^2/4\sigma_{n'm'}^4-itS_{n'm'}K_{n'm'}/\sigma_{n'm'}^2-K_{n'm'}^2}{S_{n'm'}^2/\sigma_{n'm'}^2+2/\ell^2)}\right)}_{C}\right).$$

Completion of the square of $e^{-Ar^2}e^{-Br}$ and integration over r yields

$$\sqrt{\pi/A}\exp(-B^2/4A)=\sqrt{\pi/\left(-\frac{S_{n'm'}^4/4\sigma_{n'm'}^4}{S_{n'm'}^2/\sigma_{n'm'}^2+2/\ell^2)}+\frac{S_{nm}^2}{4\sigma_{nm}^2}+\frac{S_{n'm'}^2}{4\sigma_{n'm'}^2}\right)}$$

(29)

$$\times\quad\exp\left(\frac{\left(\frac{S_{n'm'}^3t/2\sigma_{n'm'}^4-iS_{n'm'}^2K_{n'm'}/\sigma_{n'm'}^2}{S_{n'm'}^2/\sigma_{n'm'}^2+2/\ell^2}-\frac{S_{nm}t}{2\sigma_{nm}^2}-\frac{S_{n'm'}t}{2\sigma_{n'm'}^2}-i(K_{nm}-K_{n'm'})\right)^2}{-\frac{S_{n'm'}^4/\sigma_{n'm'}^4}{S_{n'm'}^2/\sigma_{n'm'}^2+2/\ell^2}+\frac{S_{nm}^2}{\sigma_{nm}^2}+\frac{S_{n'm'}^2}{\sigma_{n'm'}^2}}\right).$$

Rearrangement of Eq. (29) and multiplication with the $\exp(-C)$ from Eq. (28) and the constant term under the radical from Eq. (27) yields the closed form evaluation of the double range integrals over r'' and r

$$\exp\left(-\frac{t^2}{4\sigma_{nm}^2} - \frac{t^2}{4\sigma_{n'm'}^2}(1-R) + \left(it\frac{K_{n'm'}}{S_{n'm'}} + \frac{K_{n'm'}^2\sigma_{n'm'}^2}{S_{n'm'}^2}\right)(1-R)\right)$$

$$\times \quad \exp\left(\frac{\left(t\left(\frac{S_{nm}}{2\sigma_{nm}^2} + \frac{S_{n'm'}}{2\sigma_{n'm'}^2}(1-R)\right) + i\left(K_{nm} - K_{n'm'}(1-R)\right)\right)^2}{\frac{S_{nm}^2}{\sigma_{nm}^2} + \frac{S_{n'm'}^2}{\sigma_{n'm'}^2}(1-R)}\right)$$

$$\times \quad \sqrt{\pi / \left(\frac{S_{nm}^2}{4\sigma_{nm}^2} + \frac{S_{n'm'}^2}{4\sigma_{n'm'}^2}(1-R)\right)}$$

$$\times \quad \sqrt{\pi / (S_{n'm'}^2/4\sigma_{n'm'}^2 + 1/2\ell^2)}, \tag{30}$$

where

$$R = \left(1 + \frac{2\sigma_{n'm'}^2}{S_{n'm'}^2\ell^2}\right)^{-1}.$$

After some rearrangement Eq. (30) yields the terms inside the quadruple modal sum in Eq. (16) which are equivalent to the double range integrals over the scatterers under the approximations outlined at the beginning of this Annex.

<div align="right">

Annex C

Asymptotic forms of
intermodal correlation function

</div>

For the limit $L \gg \ell$ Eq. (18) reduces to

$$
\rho^2 = 2\pi\ell L \exp\left\{ \frac{\left(\frac{t\Delta\omega}{2}(S_{nm} + S_{n'm'}) + \frac{i}{\Delta\omega}(k_n + k_m - (k_{n'} + k_{m'}))\right)^2}{S_{nm}^2 + S_{n'm'}^2} \right\}
$$

$$
\times \exp\left\{ -t^2 \Delta\omega^2/2 - (k_{n'} + k_{m'})^2\ell^2/2 \right\}. \tag{31}
$$

The argument of the first exponent can be expanded and added to the argument of the second exponent. Multiplying through by the common denominator we obtain as the argument

$$
\begin{aligned}
\Big(& t^2 \Delta\omega^2(S_{nm}^2 + 2S_{nm}S_{n'm'} + S_{n'm'}^2)/4 \\
& + it(S_{nm} + S_{n'm'})(k_n + k_m - (k_{n'} + k_{m'})) \\
& - (k_n + k_m - (k_{n'} + k_{m'}))^2 \Delta\omega^2 \\
& - t^2 \Delta\omega^2(S_{nm}^2 + S_{n'm'}^2)/2 \\
& - (k_{n'} + k_{m'})^2\ell^2(S_{nm}^2 + S_{n'm'}^2)/2 \Big) \\
& \times \left(S_{nm}^2 + S_{n'm'}^2\right)^{-1}
\end{aligned} \tag{32}
$$

The first and the fourth line, together with the identity $\Delta\omega^2 \equiv 1/S_{n'm'}^2 L^2$ combine to give an exponent approximately of the form

$$
-\frac{t^2}{8L^2}(S_{nm}^{-2} - 2S_{nm}^{-1}S_{n'm'}^{-1} + S_{n'm'}^{-2}).
$$

The second line gives an exponent approximately of the form

$$
it(k_n + k_m - (k_{n'} + k_{m'}))/S_{nm}.
$$

The third line gives an exponent of the form

$$
-(k_n + k_m - (k_{n'} + k_{m'}))^2 L^2,
$$

and the fifth line gives the term

$$
-(k_{n'} + k_{m'})^2\ell^2/2.
$$

The meanings associated with these four terms are explained in the main body of the text.

For the limit $\ell \gg L$ Eq. (18) reduces to

$$
\rho^2 = 4\pi\ell L \exp\left\{ \frac{\left(\frac{t\triangle\omega}{2}\left(S_{nm} + 2\frac{L^2}{\ell^2}S_{n'm'}\right) + \frac{i}{\triangle\omega}\left(k_n + k_m - 2\frac{L^2}{\ell^2}(k_{n'} + k_{m'})\right)\right)^2}{S_{nm}^2 + 2\frac{L^2}{\ell^2}} \right\}
$$
$$
\times \exp\left\{ -\left(\frac{t^2\triangle\omega^2}{4}(1 + 2\frac{L^2}{\ell^2}) + i\frac{t(k_{n'} + k_{m'})}{S_{n'm'}} + (k_{n'} + k_{m'})^2 L^2 \right) \right\}. \tag{33}
$$

Expanding the denominator of the argument to the first exponent for small L^2/ℓ^2 and selectively keeping terms from the numerator to first order or lower we obtain

$$
\frac{t^2\triangle\omega^2}{4}(S_{nm}^2 + 4\frac{L^2}{\ell^2}S_{nm}S_{n'm'} + \cdots)(S_{nm}^{-2} - 2\frac{L^2}{\ell^2}S_{nm}^{-4}S_{n'm'}^2 + \cdots)
$$
$$
+ \; it(k_n + k_m)/S_{nm}
$$
$$
- \; (k_n + k_m)^2 L^2
$$

which when multiplied through (again keeping only terms order L^2/ℓ^2 and lower) may be added to the argument of the second exponent to give

$$
-\frac{t^2\triangle\omega^2}{4}(-4\frac{L^2}{\ell^2}S_{nm}^{-1}S_{n'm'} + 2\frac{L^2}{\ell^2}S_{nm}^{-2}S_{n'm'}^2 + 2\frac{L^2}{\ell^2})
$$
$$
- \; it\left(\frac{k_{n'} + k_{m'}}{S_{n'm'}} - \frac{k_n + k_m}{S_{nm}} \right)
$$
$$
- \; \left((k_n + k_m)^2 + (k_n + k_m)^2 \right) L^2,
$$

which upon insertion of the identity $\triangle\omega^2 L^2 \equiv S_{n'm'}^{-2}$ yields

$$
-\frac{t^2}{2\ell^2}(S_{nm}^{-2} - 2S_{nm}^{-1}S_{n'm'}^{-1} + S_{n'm'}^{-2})
$$
$$
- \; it\left(\frac{k_{n'} + k_{m'}}{S_{n'm'}} - \frac{k_n + k_m}{S_{nm}} \right)
$$
$$
- \; \left((k_n + k_m)^2 + (k_n + k_m)^2 \right) L^2, \tag{34}
$$

the terms of which are explained in the text.

Annex D

Expressions for small perturbation scattering from boundary impedance

Consider the following boundary condition at a rough interface in a waveguide

$$\frac{p}{\partial p/\partial n} \equiv Z$$

Let us call the lefthand side of this equation the boundary operator B which operates on the total pressure p.

In perturbation theory we expand the boundary operator about a local roughness excursion η, and let it operate on the sum of the unperturbed and scattered fields p and p_s. In the limit of zero scatterer slope we have

$$\left(B + \eta \frac{\partial B}{\partial z}\right)(p + p_s) = Z, \tag{35}$$

where

$$B = \frac{p}{\partial p/\partial z},$$

and

$$\frac{\partial B}{\partial z} \equiv 1 - \frac{p}{(\partial p/\partial z)^2}\frac{\partial^2 p}{\partial z^2}.$$

In this case Eq. (35) may be written

$$\frac{p + p_s}{\partial(p + p_s)/\partial z} + \eta\left(1 - \frac{p + p_s}{(\partial(p + p_s)/\partial x)^2}\frac{\partial^2(p + p_s)}{\partial z^2}\right) = Z,$$

or approximately

$$\frac{p + p_s}{\partial p/\partial z} - \frac{p + p_s}{(\partial p/\partial z)^2}\frac{\partial p_s}{\partial z} + \eta\left(1 - \left[\frac{p + p_s}{(\partial p/\partial z)^2} + 2\frac{p + p_s}{(\partial p/\partial z)^3}\frac{\partial p_s}{\partial z}\right]\frac{\partial^2(p + p_s)}{\partial z^2}\right) \simeq Z$$

Retaining terms of order p we have

$$\frac{p}{\partial p/\partial z} = Z,$$

while to first order in η and p_s we have

$$\frac{p_s}{\partial p/\partial z} - \frac{p}{(\partial p/\partial z)^2}\frac{\partial p_s}{\partial z} = -\eta\left(1 - \frac{p}{(\partial p/\partial z)^2}\frac{\partial^2 p}{\partial z^2}\right). \tag{36}$$

Eq. (36) may be recast to give the vertical derivative of the scattered field in term of the scattered field itself and the first and second vertical derivatives of the unperturbed pressure p

$$\frac{\partial p_s}{\partial z} = \frac{p_s}{Z} + \eta \left(\frac{(\partial p/\partial z)^2}{p} - \frac{\partial^2 p}{\partial z^2} \right).$$ (37)

Now we may use Green's third identity to formulate the scattered pressure received at any point in the waveguide in terms of the scattered field and its vertical derivative along the boundary of the waveguide

$$\begin{aligned} p_s &= \frac{1}{2\pi} \int dS \left(p_s \frac{\partial G}{\partial z} - G \frac{\partial p_s}{\partial z} \right) \\ &= \frac{1}{2\pi} \int dS \left(p_s \frac{G}{Z} - G \frac{\partial p_s}{\partial z} \right), \end{aligned}$$ (38)

which upon the insertion of Eq. (37) yields

$$p_s = \frac{1}{2\pi} \int dS \, G\eta \left(\frac{\partial^2 p}{\partial z^2} - \frac{(\partial p/\partial z)}{Z} \right).$$ (39)

Eq. (39) may be written in final form by using the following far field approximations for the unperturbed waveguide

$$G(z, z_b; r) = \frac{ie^{-i\pi/4}}{\sqrt{8\pi}\rho(z_b^+)} \sum_m \phi_m(z_b)\phi_m(z) \frac{e^{ik_m r}}{\sqrt{k_m r}},$$ (40)

and

$$p(z_b; r) = e^{-i\pi/4}\sqrt{2/\pi} \sum_n a_n \phi_n(z_b) \frac{e^{ik_n r}}{\sqrt{k_n r}},$$ (41)

where a_n are the modal amplitude coefficients excited by the source. Inserting Eqs. (40) and (41) into Eq. (39) we obtain the final expression for the scattered field obtained on the receiver as a function of the mode shape functions and wavenumbers of the waveguide and the roughness η

$$\begin{aligned} p_s(z) &= \frac{1}{4\pi^2 \rho(z_b^+)} \int_0^{2\pi} d\theta \int_0^\infty dr \sum_n \sum_m a_n \phi_m(z_b)\phi_m(z) \frac{e^{i(k_n + k_m)r}}{\sqrt{k_n k_m}} \\ &\quad \times \left. \eta(r, \theta) \left(\frac{\partial \phi_n/\partial z}{Z} - \frac{\partial^2 \phi_n}{\partial z^2} \right) \right|_{z=z_b^+} \end{aligned}$$ (42)

Security Classification		Project No.
UNCLASSIFIED		042-4

Document Serial No.	Date of Issue	Total Pages
SR-301	October 1998	66 pp.

Author(s)

LePage, K.D.

Title

Bottom reverberation in shallow water: coherent properties as a function of bandwidth, waveguide characteristics and scatterer distributions.

Abstract

Scattering physics are often modelled using the Helmholtz equation for computational reasons. Likewise, propagation loss to and from scattering regions are often treated in a like manner. The usual approach for generating reverberation time series therefore requires a numerical Fourier synthesis which can obscure the physics of reverberation phenomenology. Here we model the reverberation process approximately using normal modes and perform the Fourier synthesis explicitly under a narrow band approximation. The modes area allowed to interact with the bottom individually, but the interaction of the modes at the bottom is also retained. Therefore the approach allows pathological propagation phenomena such as convergence zones to be explicitly modelled. As a natural result of the broadband nature of the analysis, the interaction of the modes with each other at the bottom is seen to be governed by the bandwidth of the analysis and the dispersive properties of the waveguide. The result is that modes which interact coherently at bottom patches at early time may decorrelate at late times, in ways which are determined by the mean propagation physics of the waveguide and the reverberation analysis band.

In the interests of keeping the approach as general as possible, the physics of the bottom scattering process are specified by the user. These physics are supplied in the form of local bottom scattering functions, which will generally be related to the mode shape functions and their derivatives at and in the bottom, which are sensitive to the detailed bottom structure and the incident grazing angles of each mode. The approach makes it possible to model several of the more popular bottom scattering models, such as perturbation theory and Lambert's law, within the framework of a general reverberation model. All scattering is assumed to be weak, so that a small imaginary part of the model eigenvalues is sufficient to account for energy loss due to scattering, and local, so that the field scattered at any particular part of the bottom is due only to the bottom properties at that particular point. This later approximation serves as a restriction on the ability of the model to accommodate large scale scatterers such as facets or other target type features, but is useful for modelling clutter, the intended objective.

Keywords

Initial Distribution for Unclassified SR-301

Ministries of Defence		Scientific Committee of National Representatives	
DND Canada	10	SCNR Belgium	1
CHOD Denmark	8	SCNR Canada	1
DGA France	8	SCNR Denmark	1
MOD Germany	15	SCNR Germany	1
HNDGS Greece	12	SCNR Greece	1
MARISTAT Italy	9	SCNR Italy	1
MOD (Navy) Netherlands	12	SCNR Netherlands	2
NDRE Norway	10	SCNR Norway	1
MOD Portugal	5	SCNR Portugal	1
MDN Spain	2	SCNR Spain	1
TDKK and DNHO Turkey	5	SCNR Turkey	1
MOD UK	20	SCNR UK	1
ONR USA	34	SCNR USA	2
		French Delegate	1
		SECGEN Rep. SCNR	1
NATO Commands and Agencies		NAMILCOM Rep. SCNR	1
NAMILCOM	2		
SACLANT	3	**National Liaison Officers**	
CINCEASTLANT/			
COMNAVNORTHWEST	1	NLO Canada	1
CINCIBERLANT	1	NLO Denmark	1
CINCWESTLANT	1	NLO Germany	1
COMASWSTRIKFOR	1	NLO Italy	1
COMSTRIKFLTANT	1	NLO Netherlands	1
COMSUBACLANT	1	NLO Spain	1
SACLANTREPEUR	1	NLO UK	1
SACEUR	2	NLO USA	1
CINCNORTHWEST	1		
CINCSOUTH	1		
COMEDCENT	1		
COMMARAIRMED	1		
COMNAVSOUTH	1		
COMSTRIKFORSOUTH	1	**Sub-total**	199
COMSUBMED	1		
NC3A	1	SACLANTCEN	30
PAT	1		
		Total	229